UNIVERSIDAD CARLOS III DE MADRID
ESCUELA POLITÉCNICA SUPERIOR

BOUNDARY LAYER CONTROL BY MEANS OF DBD PLASMA ACTUATORS

Bachelor Thesis

Author

Edgar Martín Nieto

Leganés, June 2016

Department of Aerospace Engineering
ESCUELA POLITÉCNICA SUPERIOR

BOUNDARY LAYER CONTROL BY MEANS OF DBD PLASMA ACTUATORS

Bachelor in Aerospace Engineering

Author

Edgar Martín Nieto

Supervisor

Yacine Babou

Leganés, June 2016

Acknowledgements

I would like to thank my tutor, prof. Yacine Babou, for all the effort and continuous support he has given to me throughout the realization of this work not only on the academic side, and the patiente, understanding and dedication he has proven on this period. Needless to say, he has helped me to grasp the matter of plasma physics, a humongously extent topic.

I would like also to thank prof. Pablo Fajardo for the support on Fluent handling, and the support given when all the data dissapears in the blink of an eye.

This work goes as well to those friends who have stayed with me in this four years, no matter which the situation was, and who have teached me the other side (dark side) of university life.

Last but not least, thanks to all my family for the constant thoughts they have towards me, even when separated by the distance, and without whom I would not have had the strength and motivation to complete this degree. Special thanks to Miguel Andrés and my grandfather, for constantly pointing me towards the bright side of life, *Ad astra per aspera.*

Me gustaría agradecer a mi tutor, prof. Yacine Babou, por todo el esfuerzo y continuo apoyo que me ha dado a lo largo de la realización de este trabajo no solo académicamente, así como por la paciencia, entendimiento y dedicación que ha demostrado en este periodo. Ni que decir tiene, me ha ayudado a captar por encima la física de plasmas, tema de enorme extensión.

Me gustaría agradecer también al prof. Pablo Fajardo por el apoyo en el manejo de Fluent, y el apoyo cuando los archivos desaparecían sin previo aviso.

Este trabajo está dedicado tambien a aquellos amigos que han estado a mi lado en estos cuatro años, sin importar la situación; y que me han enseñado el otro lado (lado oscuro) the la vida universitaria.

Y por último pero no menos importante, gracias a mi familia por las preocupaciones contínuas a pesar de la distancia, y sin los que no habría tenido la fuerza y motivación para terminar esta etapa. Gracias especiales a Miguel Andrés (Mimi) y mi abuelo Custodio, por apuntarme siempre al lado positivo de la vida. *Ad astra, per aspera.*

Abstract

In this thesis a new aerodynamic model to simulate the behavior of Dielectric Barrier Discharge actuator has been studied. For this task, two different models have been merged in order to provide a more accurate one. The model has been implemented using commercial computational fluid dynamics software through built-in tools. Different configurations have been followed up in order to validate the model.

During this validation, the phenomena ocurring in the different configurations has been studied, remarking on the ability of the modelled devices to have an effect on low-speed flows, with different extent.

The model has the aim of improving and easing the computational side of this actuators, that tend to couple electric, fluid an kinetic phenomena; with the scope of investigating its potential in different applications in a simpler way.

Contents

List of Figures

List of Tables

Introduction

Boundary layer control is of high interest and has led to several studies within the aerodynamic and stability scopes, mainly due to the detrimental effects of separation, such as a reduction on lift generated by an aerodynamic surface or buffeting phenomena. Flow control extends not only to normal airfoil and wing surfaces, but also to internal engine blades, ducts and diffusers, with different strategies followed to mitigate its effects.

In this section a brief introduction to the developement of the matter of flow control with EHD will be described, with the different methods and strategies followed to actuate on the boundary layer on general wings and the recent work carried out on electrical actuators. In the recent years interest has sparked for these last actuators, as they promise instant actuation with low power consumption.

1.1 State of the art

Boundary layer control methods may be splitted in two categories:

- Passive methods changing the geometry of the surface mainly through mechanical means, and using the properties of the shape of the body.

- Active methods, where the properties of the fluid are directly acted without changing the surface. This category includes, but is not limited to, sucking or blowing jets, use of MEMS (Micro-electro-mechanical systems) and Electrohydrodynamic (EHD) actuators .

The most extended means are passive, and although mechanical devices are effective, they require complex parts that affect reliability, add weight and are prone to noise and vibration generation. An alternative solution is the use of EHD's, that using an electric field they ionize and accelerate the air laying above. This has been demonstrated to work for Low Reynold's number applications [5, 6].

The most promising actuator currently being investigated is the Dielectric Barrier Discharge (from now on, DBD) plasma actuators, as they prove for more than one decade its effectiveness [4]. Up to now, only partial models have been developed to describe the working principle of this actuators [7, 8, 9, 10].

The exact modelling of DBD's is not tractable due to the high coupling between Navier-Stokes equations for fluids, Poisson equations for electrostatics and the different species taking place in the problem, such as negative and positive ions or electrons. A simpler model was proposed by Soloviev [1] that only acts on the momentum equation of the Navier-Stokes fluid equations. This model does not provide a full distribution of the force, but the total thrust applied by the model.

Alternatively, K. P. Singh et al. [11] show an empirical model for the distribution of the thrust on a plasma actuator, with good results in shape but which calculated thrust does not adjust to real results. To solve this, L. del Amo [12] proposed and carried on a combination of this distribution normalized with the total thrust model proposed by Soloviev.

1.2   Objectives

The objectives of the present work are to implement, simulate and check the validity of a simple model to mimic the resulting effect of a DBD actuator in CFD simulations, disposing them in different configurations and checking them with bibliography's empirical data to check the validity of the model. This implemented model may simplify the computational times and resources involved, allowing for implementation in more complex systems such as wings with high lift devices.

For this reason, there are already models that represent accurately how the force and the distribution of the force acts in a plasma actuator, but they are either incomplete or have not being validated with experimental results. If the present study is able to develope a valid model for simulations of this actuators, it would open up the possibilities for full scale simulations and future device implementation for a wide variety of applications, ranging from aerodynamic effects to stability and control of aircraft, in wake of previous del Amo's work.

SDBD Force Models

In the present chapter the fundamentals of a single Surface DBD (SDBD) operations are introduced and the model adopted to predict the thrust generated is presented. The following investigation will be based on the model previously porposed by del Amo to predict the thrust generated by a SDBD operating in the dry air.

This model has been obtained by combining two different models indentified in the literature and described hereafter.

2.1 Operation principle of SDBD's

In general, a SDBD plasma actuator is arranged as two electrode plates displayed in assymetrical manner, one above a dielectric surface and the other buried below it, integrated or encapsulated. The second electrode is usually placed right after the end of the upper electrode in the downstream direction or letting a gap. These electrodes are connected in series to a RF, high voltage power supply. Typically, the power supply provides on the order of ten thousands of volts and at a frequency of the order of ten thousands of Hertz, suitable to maintain a plasma discharge.

A typical configuration of SDB is shown in figure 2.1. This type of actuator produces a flow about few meters per second when operated at 10 kV, 10 kHz. However, the performances (e.g. velocity, thrust) are strongly dependent on various parameters of the design: Dielectric thickness, dielectric properties, length of the upper and lower electrodes, length of the gap between electrodes, geometry of exposed electrode, shape function of the applied power inputs...

Effectively, these actuators act as a capacitor for low values of frequency (i.e. before the discharge occurs), with small current leakages at the operational range that correspond to the ionization of the air (for more information, see Reference [1, 13].

When the upper electrode is subjected to a sinusoidal wave of voltage, an electric field developes around it, effectively developing ion species charged and electrons
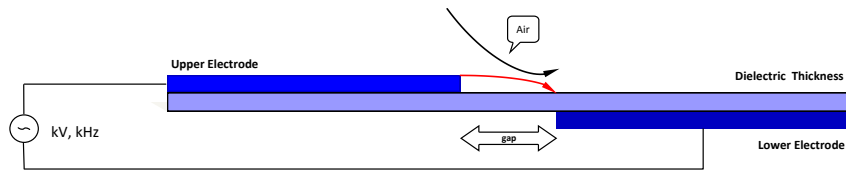
Figure 2.1: Schematics of flow induced by a single SDBD actuator. The plasma (simbolized in red) covers the exposed air between upper and lower electrodes.

that move through this electrical field according to their polarity. To maintain the discharge it is needed to have a transient electric potential monotonically increasing. Therefore as a rule a DBD plasma is generated with a sinus voltage function shape.

The mechanism of thrust production is yet not fully understood. The simulation remains a difficult task, since it requires coupling Navier-Stokes equations for fluid mechanics with Poisson equation for electric field and with a kinetic model to account for the reactive aspects.

Following several authors [8, 14, 15] this process of conversion of electrical power to thrust takes place in two steps: an excitation phase that ionizes the fluid (through glow discharges or streamer discharges, for negative and positive electrode polarity respectively) and a second phase where no more ionization occurs and the ions move to create a body force. In order to bypass the difficulties inherent to the simulation of the thrust resulting from a DBD, a simplified model will be used instead.

2.2 Soloviev's model

The aim of Soloviev in his work [1] was to estimate analytically the force produced by a SDBD by means of a phenomenological model with experimental data and applying plasma physics theory, in order to define a simple analytical expression well suited for coupling with Navier-Stokes equations.

This model states that the main contribution for the force comes from the negatively charged species, that later recombine or deposit in the dielectric surface. By doing an analysis of the discharge of electrons, probability of ion formation and time of residence inside the electric field of said ions, the force can be integrated knowing the geometry of the problem and the operating conditions. The equation to be integrated is:
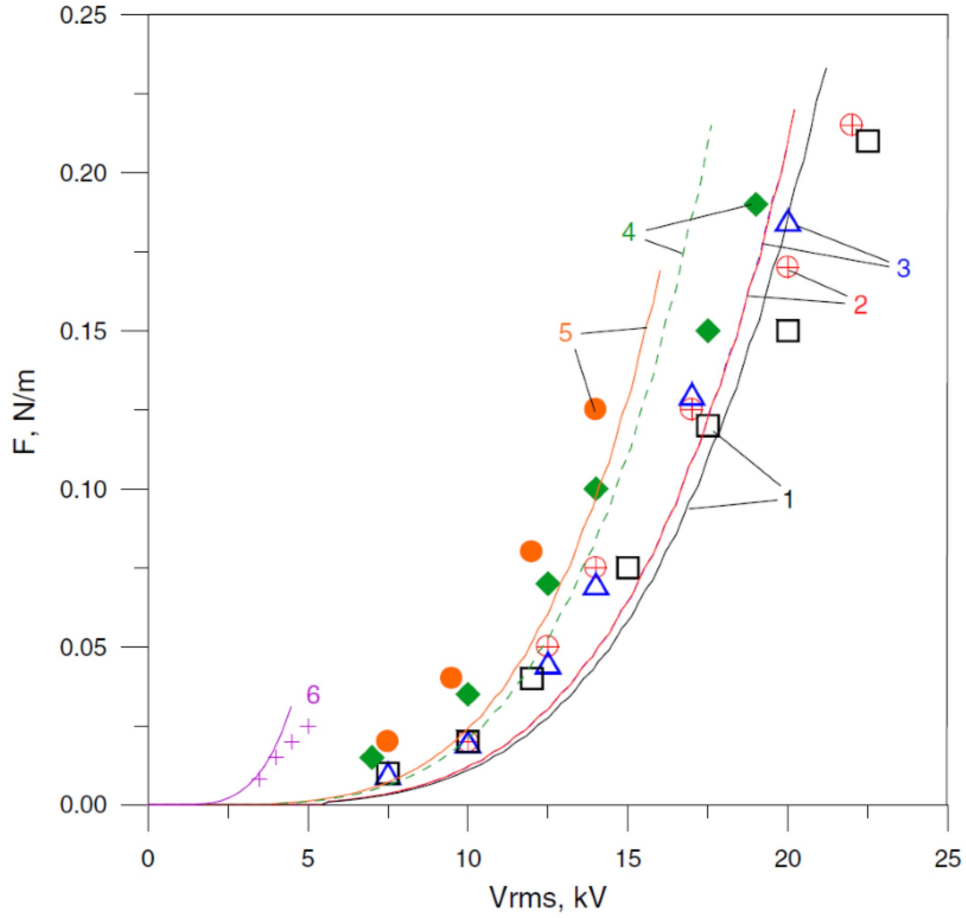
Figure 2.2: Theoretical estimation of the thrust per unit electrode length (lines) against experimental data [1] (symbols) for 1—Teflon ($\epsilon = 2$), d = 6.35mm, f_v = 2.1kHz; 2—Derlin ($\epsilon = 3.5$), d = 6.35mm, f_v = 2.3kHz; 3—quartz ($\epsilon = 4.2$), d = 6.35mm, f_v = 2.3kHz; 4—Teflon($\epsilon = 2$), d = 3.18mm, f_v = 2kHz; 5—Macor ($\epsilon = 6$), d = 3.18 mm, f_v = 2.3 kHz; 6—Kapton (ϵ=3.9),d=0.15mm,f_v =4.4kHz; V_{rms}=V_0/1.7.

$$F \approx \frac{1}{T_V} \int_{\Delta t_0}^{T_V/4} q_n(t) E_{xl}(t) \mathrm{d}t \tag{2.1}$$

Soloviev integrates this equation in the frame of several assumptions and obtains the following expression (see [1] for details):

$$F \approx 2.4 \times 10^{-10} \alpha_l^4 \frac{f_V(kHz)}{d(cm)} \left(\frac{9V_0}{4\Delta V_c} \right)^4 \left(1 - \frac{7\Delta V_c}{6V_0} \right)^4 \left(1 - exp\left(-\frac{1}{4f_V \Delta \tau_q} \right) \right) \tag{2.2}$$

Where f_V denotes the frequency applied, d is the thickness of the dielectric, V_0 the applied voltage peak-to-peak, ΔV_c the normal falldown of cathode voltage, α_l a fitting parameter, usually set to unity; and $\Delta \tau_q$ is the residence time of negative ions inside the acceleration volume. This parameter can be estimated using:

$$\Delta \tau_q \approx \frac{\alpha_l^2 V_0}{8 \times 10^5 \varepsilon \Delta V_c} \tag{2.3}$$

This equation is in good agreement with the experimental results conducted for a fixed geometry with different dielectrics. The results includes dependence on the dielectric constant, and explicitely on the thickness, voltage and frequency applied. Figure 2.2 shows the computed values with respect to experimental data. In the followings, Soloviev's recommendations on the parameters to be used will be followed, stated as $\alpha_l = 1$, $V_0 = 600V$, $\Delta \tau_q = 100 \cdot 10^{-6}$ s.

Soloviev's model is only able to give a global thrust, and does not give any insights on the distribution of said thrust. Furthermore, although the trends in Soloviev's work are followed, the thrust generated is not quantitatively accurate with the experimental results. For instance, looking at the values from 2.2, it is regarded that the calculated values lay below the experimental values for the same cases, of up to double in some cases.

2.3 Singh model

The aim of the investigation reported in Singh [11] was to produce a satisfying description of the distribution of the body forces produced by a SDBD. this work was based on previous exact computations (solving Navier-Sotkes, Poisson and kinetic equations for several species), and a relationship between EHD force and problem parameters has been approximated.

The resulting expression was fitted on a set of exact computations, and the expression is given by:

$$\vec{F}(x,y) = F_{x0}\phi_0^4 \exp\left[-\left(\frac{x - x_0 - (y - y_0)}{y}\right)^2 - \beta_x(y - y_0)^2\right]\hat{\imath}$$

$$+ F_{y0}\phi_0^4 \exp\left[-\left(\frac{x - x_0}{y}\right)^2 - \beta_y(y - y_0)^2\right]\hat{\jmath} \tag{2.4}$$

Where F_{x0}, F_{y0} are average thrust parameters obtained from the numerical solution of air-plasma equations, ϕ_0 is the applied voltage and β_x, β_y are function

of the dielectric material and adjusted to match the model to the velocity of the simulations. Following this reasoning, the parameters from the equations will be maintained: F_{x0}, F_{y0} are set to 2.6 and 2.0 respectively, and $\beta_x = 8 \cdot 10^5$, $\beta_y = 10^7$ as suggested by Sighn. The distributions along the space can be seen in figures 2.3.

However, when trying to reproduce the results given by Sighn et al. with the approximated force they did not match feasible velocities, reaching up to 800 ms^{-1} for non-compressible still air of density 1.225 kgm^{-3} Therefore, it is not a reliable model in terms of global thrust (also said by the authors), but reliable on the shape.

Moreover, this model can only be applied to a model with an upper electrode of 2mm, lower electrode of 4mm an a gap of 2mm, as studied by them. Therefore, a refitting of the parameters must be done to be applied to other geometries.

This is an important point compared to other models such as Shyy et al., that propose a triangular distribution, for the fact that the application of the model does not depend on an arbitrary volume (such as a triangle or rectangle) where the force is applied, but can be applied everywhere provided the scale and geometry of the problem.
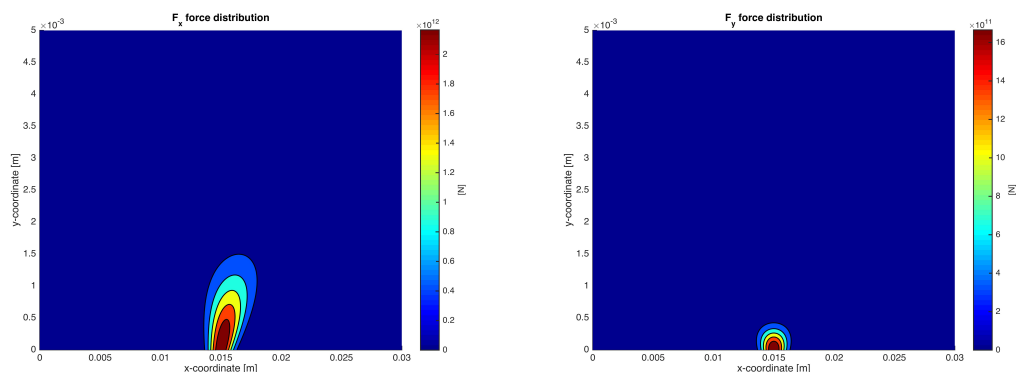
Figure 2.3: Force contour maps for F_x and F_y distributions respectively.

2.4   Merged model

Regarding this two last models, none of them is able to describe the EHD distribution, giving only either the global thrust with no distribution or the distribution without the ability to predict fair thrust. For this reason, L. del Amo [12] decided to improve the previous models by merging them into one model.

The approach followed by del Amo was to normalize the Singh equation and then to multiply by Soloviev's theoretical value of the force to obtain a model which pre-

dicts accurately forces imparted to the actuator *and* approximation of distribution of forces around it.

To do this, del Amo integrated the force imparted by the model along the simulation volume. The limits of integrations would be considered to be at infinity, although practically a finite volume has to be set. This was done in increasing steps until a steady value of the results was obtained for each component. The integral to be performed is:

$$\vec{F} = \iint F_{x0}\phi_0^4 \exp\left[-\left(\frac{x - x_0 - (y - y_0)}{y}\right)^2 - \beta_x(y - y_0)^2\right]\hat{\imath}$$
$$+ F_{y0}\phi_0^4 \exp\left[-\left(\frac{x - x_0}{y}\right)^2 - \beta_y(y - y_0)^2\right]\hat{\jmath} \ \mathrm{d}x\mathrm{d}y \tag{2.5}$$

Parameter ϕ_0 was set to unity for the distribution not to be dependent on the voltage, as this parameter will come from the Soloviev's term. Therefore, the expression combined would be:

$$\vec{F}(x, y) = F_{sol}(d, V_0, f_V) \cdot \frac{\vec{f}_{sighn}(\vec{p}_0, \vec{p}, \vec{F}_0, \vec{\beta})}{\|\vec{F}\|} \tag{2.6}$$

Where $\vec{p}_0$, $\vec{p}$ denote the initial position of the actuator and the point to be calculated in cartesian coordinates. The final expression becomes:

$$\vec{T}_0 = 2.4 \cdot 10^{-10}\alpha_l^4 \frac{f_V(kHz)}{d(cm)}\left(\frac{9V_0}{4\Delta V_c}\right)^4\left(1 - \frac{7\Delta V_c}{6V_0}\right)^4\left(1 - exp\left(-\frac{1}{4f_V\Delta\tau_q}\right)\right)$$
$$\cdot \frac{1}{\|\vec{F}\|} \cdot \left\{r \cdot \exp\left[-\left(\frac{x - x_0 - (y - y_0)}{y}\right)^2 - \beta_x(y - y_0)^2\right]\hat{\imath}\right.$$
$$\left. + \exp\left[-\left(\frac{x - x_0}{y}\right)^2 - \beta_y(y - y_0)^2\right]\hat{\jmath}\right\} \tag{2.7}$$

$$r = \frac{F_{x0}}{F_{y0}} \tag{2.8}$$

At the resulting EHD force distribution expression, it is explicitly dependent on various parameters, related to the configuration (dielectric thickness) of the SDBD and operating settings (frequency and voltage).

Moreover, this model includes also dependencies to specific parameters that depend on the arregement setting but for which constant values are taking into account

following the recommendations of the authors for the specific models. These values are herafter listed, and will be followed for the rest of the work:

$$\alpha_l = 1$$

$$\Delta V_c = 600 \ V$$

$$\Delta \tau_q = 10^{-4}$$

$$F_{x0} = 2.6$$

$$F_{y0} = 2$$

$$\beta_x = 8 \cdot 10^5$$

$$\beta_x = 10^7$$

$$\|\vec{F}\| = 7.5359 \cdot 10^{-6}$$

For further improvement of the model it could be worthwhile to evaluate the importance of those parameters and the sensibility to different control parameters.

Numerical solver assesment

After presenting the selected model and doing the conversion for them, their validity must be checked. This will be done using the model in a CFD solver with different geometries arranged in several configurations, and checking them with the available experimental data.

Therefore, in this chapter the explanation on how the different simulations were performed will be explained in detail for future peer review.

The methodology to be followed up will be to implement a body force term in the momentum Navier-Stokes equations equal to that of the merged model from del Amo (From now on it will be called Merged model). Once the Merged model is implemented, the simulation will be run until convergence, and the results will be extracted and analyzed. In figure 3.1 the process is explained:

The input parameters of the problem are the kinematics and dynamics of fluids (Navier-Stokes equations), the geometry to be solved (arrangement of control volume and actuators) and the model for the actuators. Once the computational error of the Navier-Stokes momentum equations is lower than 10^-8, the computation can be considered converged and the results of velocity profiles at different positions and total forces will be extracted. This will be later compared with literature experimental results to check the validity of the model.

3.1 CFD Solver

The CFD solver to be used will be Fluent, a program integrated into the ANSYS Suite, due to its availability at the department. This suite is intended for multiphysics simulations of structures, fluid dynamics and electromagnetics through finite difference method. The fluid is discretized in multiple cells, and the equations involved approximated by a numerical scheme. Then, the system is solved iteratively until a reasonable difference between the previous and the new calculations is obtained.
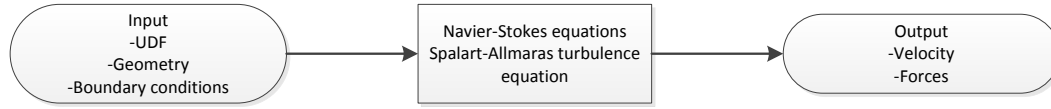
Figure 3.1: Diagram showing the work of Fluent.

An integration of the body force must be performed. For this purpose, Fluent provides a tool to alter different parameters of the program and the equations, through User Defined Functions (from now on, UDFs). These UDFs are programmed in C code with the parameters that model the fluid to be calculated, effectively allowing for the user to simulate any type of behavior.

In particular, a change in the equation of momentum has been done, in accordance to the previously exposed theory. This function takes as input parameters the fluid position of the cell to be calculated, checks which is the reference system to be used by the fluid, calculates the force to be applied at that specific cell and passes it to the main computing thread of the program.

3.2 Problem parameters

Model equations

Both problems were solved using Navier-Stokes equations with the Spalart-Allmaras turbulent model, that is the recommended method to simulate low-Reynolds, turbulent flows. Therefore, the problem has three equations:

Navier-Stokes equations

$$\frac{\partial \rho}{\partial t} + \nabla \cdot (\rho \vec{v}) = 0 \tag{3.1}$$

$$\frac{\partial}{\partial t}(\rho \vec{v}) + \nabla \cdot (\rho \vec{v} \vec{v}) = \nabla p + \nabla \cdot \overline{\overline{\tau'}} + \rho \vec{f_m} \tag{3.2}$$

Spalart-Allmaras model

$$\frac{\partial}{\partial t}(\rho\tilde{\nu}) + \frac{\partial}{\partial x_i}(\rho\tilde{\nu}u_i) = G_\nu + \frac{1}{\sigma_{\tilde{\nu}}}\left[\frac{\partial}{\partial x_j}\left\{(\mu + \rho\tilde{\nu})\frac{\partial\tilde{\nu}}{\partial x_j}\right\} + C_{b2}\rho\left(\frac{\partial\tilde{\nu}}{\partial x_j}\right)^2\right] - Y_\nu \quad (3.3)$$

Which is a transport equation where $\tilde{\nu}$ is a viscosity-like term, G_ν is the production of turbulent viscosity, and Y_ν is the destruction of turbulent viscosity that occurs in the near-wall region due to wall blocking and viscous damping. $\sigma_{\tilde{\nu}}$ and C_{b2} are the constants and ν is the molecular kinematic viscosity.

Note that for the momentum equation two directions are taken into account, thus developing into four total equations. The model is considered to be steady, non-viscous, quiescent air of constant density.

Boundary conditions

The boundary conditions of the problem where set to pressure-outlet for left, right and upper boundaries. This is a condition where the fluid pressure matches the ambient pressure on the limiting cells, without changing the velocity of the fluid. This simulates the conditions of open test bench from the papers.

The lower limit was set to wall condition, where there is no mass or momentum transfer from and to the boundary. Furthermore, the tangential velocity of the fluid is also 0 on the wall, complying with the non-slip condition.

For the case study of other applications, the inlet was set to velocity-inlet to be able to introduce a velocity at an ambient pressure, and evaluate the efficiency of the actuator on different conditions.

UDF inclusion

To implement the model, Fluent provides a UDF tool that allows to include a body force on the equation (namely $\vec{f_m}$). This force is applied to every cell according to the conditions specified in the code.

The inclusion is done in two steps. First, Soloviev's term is calculated apart and included as a constant parameter, as the function does not allow any input parameter once it is set on the fluid. Once the term is calculated, it is multiplied by the distribution, using the constants del Amo used in her work for nondimensioning the distribution.

To implement the distribution in any desired angle, a rotation must be performed. By default Fluent takes as input parameters of the UDF the position relative to the global coordinate system of the center of the cell to be calculated. If the actuator is to be rotated, the actual force it will experience would be of that of a non-rotated point located in an equivalent position. The rotation with an angle θ is:

$$\vec{x}' = x_0 + (\vec{x} - x_0) \cdot \cos(\theta) - (\vec{y} - y_0) \cdot \sin(\theta) \tag{3.4}$$

$$\vec{y}' = y_0 + (\vec{x} - x_0) \cdot \sin(\theta) + (\vec{y} - y_0) \cdot \cos(\theta) \tag{3.5}$$

Where x_0, y_0 corresponds to the placing point of the actuator, θ is defined positive clockwise. These parameters are then evaluated in del Amo's model, obtaining the force applied in the local coordinates.

This force is retrieved by the UDF in the global coordinate system as well, so a conversion of the force back to that coordinate system must be performed as well. This is given by the transformation:

$$\vec{F}_x = \quad \vec{F}'_x \cdot \cos(\theta) + \vec{F}'_y \cdot \sin(\theta) \tag{3.6}$$

$$\vec{F}_y = -\vec{F}'_x \cdot \sin(\theta) + \vec{F}'_y \cdot \cos(\theta) \tag{3.7}$$

Figures [Include figures showing rotation] explain this change visually for a quick comprehension. In Annex [Insert annex] an example of this code is presented as an example.

Convergence criteria

To consider the fluid converged two criteria have been followed. The first criterion is the convergence of residuals. These are the difference in the Navier-Stokes equations from a computational step to the next one. When this difference is small, the fluid can be considered to reach a steady solution. These residuals have been set to 10^{-5} for mass conservation equation and 10^{-9} for the x-velocity, y-velocity and turbulent kinematic viscosity (nut).

The other criterion followed was to stablish a net coefficient to be studied, namely upward force or side force (cl & cd). These coefficients would vary when iterations were computed, and once they settle down (i.e. they become constant) the fluid could be considered to be converged.

In practice, a balance between both was made, applying usually the first one and

checking if the second held.

In some of the configurations, the fluid became unstable and entered a resonance in the residuals. This was caused due to the fact that the fluid was not steady anymore, but had transient behaviors. A compromise solution was done for these cases, that were near to convergence, taking as a valid solution one of the states.

Application 1: In-series actuators

4.1   Arrangement principle

As the first orientation followed to assess the performance of the model adopted and described in previous chapters, which deals merely with the effect of only one actuator, in this chapter an arrangement of several of them placed on a surface is evaluated.

In that frame, the quiescent flow of air is actuated by serveral actuators evenly distributed. This has been studied experimentaly by various authors, such as Moreau et al. [2]. With this arragement is possible on one side to promote accumulation and on the other broadening of the actuated flow at the surface vicinity, to target larger scale applications.

The proposed calculations are dedicated to assess the potential of the model to predict these two phenomena. The typical configuration corresponding to this situation is depicted in figure 4.1 and will be considered in the followings.

It is important to note that Moreau used wires as an upper electrode for his experimental case rather than flat plates, as well as a mixing of dielectrics. This has an observable change in the distribution of the fluid around the actuator, as shown by his own work, and therefore the numerical results obtained may be dissimilar to this experimental case. Nevertheless, the rest of the parameters have been followed up.
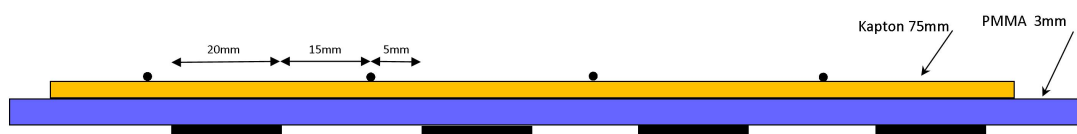

Figure 4.1: In-series actuators arrangement as in [2]

4.2   Geometry of the problem and parameters

This set of actuators has been simulated on a flat surface all facing the downstream direction. Four of them, with a gap of 40mm in between each, are set with equal amount of thrust applied to them. The global thurst is calculated using the parameters, Table 4.1 shows the cases studied, in accordance to the experminetal setup documented in [2], and the theoretical thurst each actuator is inflicting by substitution of the parameters in Soloviev's term.

Voltage $[kV]$	Applied force $[\text{N·m}^{-1}]$
16	$7.7635 \cdot 10^{-3}$
20	0.019657
24	0.041755

Table 4.1: Applied forces for 1kHz, 0.3075 cm dielectric

The volume used to simulate this geometry is 1.5×16 cm, with the first actuator placed 2 cm from the left side. The mesh is generated with 60000 elements, with a bias factor of 7.5 (ratio of larger vs. shorter distance) of vertical resolution towards the lower wall. With this, better definition of the forces in this region is achieved, modeling the transfer of momentum in a more accurate way for each cell. The time needed for each iteration is around one second, converging at around 10^4 iterations.

4.3   Results and Analysis

It is important to keep in mind, as mentioned in chapter 2.1,that the shape of the electrodes and particularities of dielectric materials will not be replicated, hence it is already expected that the following calculations may differ from experimental data (obtained with cylindrical upper electrode and inhomogeneous dielectric layer).

However, as Soloviev states, the dielectric constant has an implicit effect on the force applied and the maximum efficiency, which is regarded as constant. Therefore, although mixing of dielectrics is present, in first approach is regarded as having no effect but the associated to its thickness. The computational results obtained for the geometry described are compared in the following figure 4.2 for the three cases, superposed to the expermental values of Moreau.
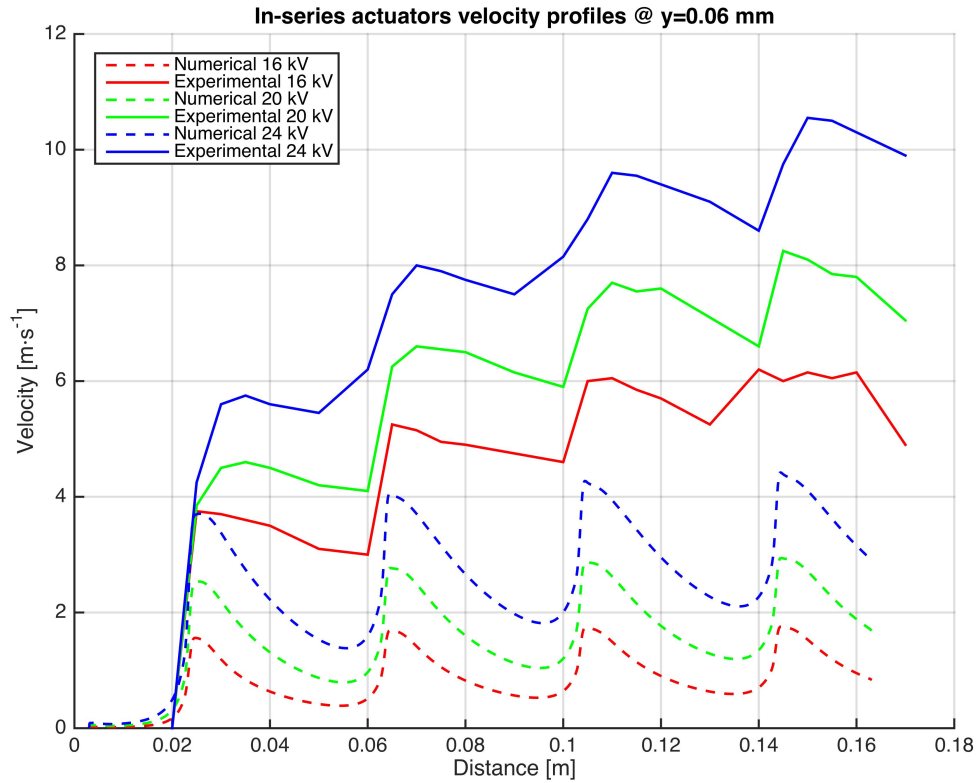
Figure 4.2: In-series actuators for 1 kHz, 3 mm dielectric thickness.

It is seen that for the three configurations in figure 4.2, although the trends were followed, the corresponding velocities do not match. The possible sources of discrepancies are:

- The type of actuator used in the experimental results is not the same as the one used for the numerical calculations.

- The Soloviev term does not predict in an exact way the actual thrust given by the actuator, as seen before in chapter 2.1.

- The distribution of the force is not fitted to the parameters of the actuators, i.e. the actuator acts in a very narrow region in the x direction.

Comparing the results of Soloviev (in figure 2.2), for the range of study the disagreement was about twice the power. For this purpose, the results from the 24 kV calculation were compared to those from the experimental results of the 16 kV calculation. The results are presented in figure 4.3.
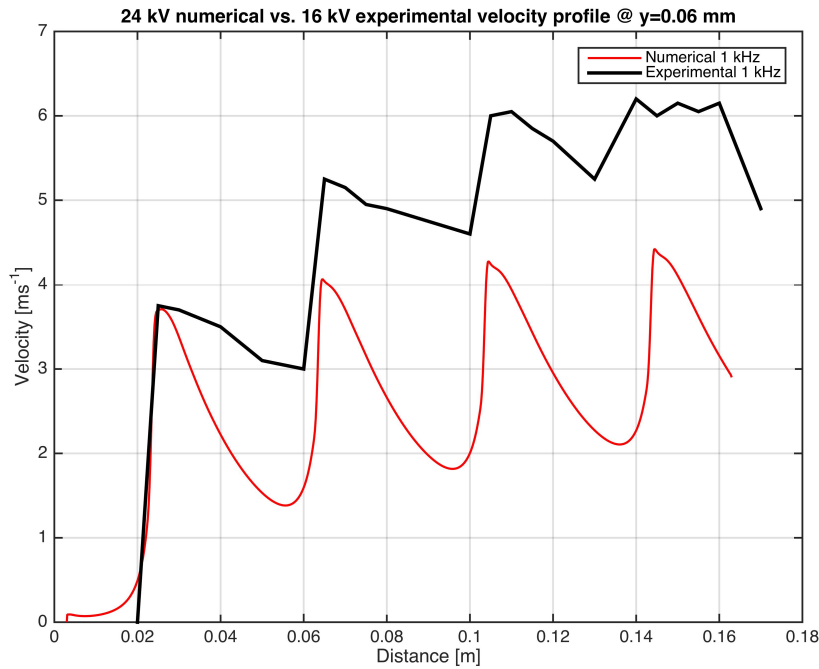
Figure 4.3: Inline actuators for 24 kV, 1 kHz, 3 mm dielectric thickness compared to 16 kV experimental results.

In it, it is seen that for the first actuator the velocity at the designated height is the same for both experiments and numerical simulations. However, the velocity in the numerical simulation quickly decays, while in the experimental setup is slower. This could be due to the fact that the experimental actuator distributes the thrust along the x direction much elongated than the used actuator, maintaining higher velocities along that direction. The cumulative effect therefore is higher, having a higher trend along all the actuators. Looking at this graph can be appreciated that a refitting of the Singh model is needed in order to predict the inter-electrode behavior of the arragement.

In the next step the height of greatest x-velocity was extracted, and how the fluid behaved at that best height was analized. The results for each case are displayed in figures 4.4, 4.5 and 4.6, where a larger minimum velocity between actuators is present, and nearly no improvement on the maximum velocity is present. This velocity shows more accordance to the experimental values, as the relaxation velocities do not decay as faster.

Comparing the graph to the height used by Moreau, the height of measurment of 0.6 mm is representative, although larger velocities are present in higher layers after the actuators (figure 4.7).
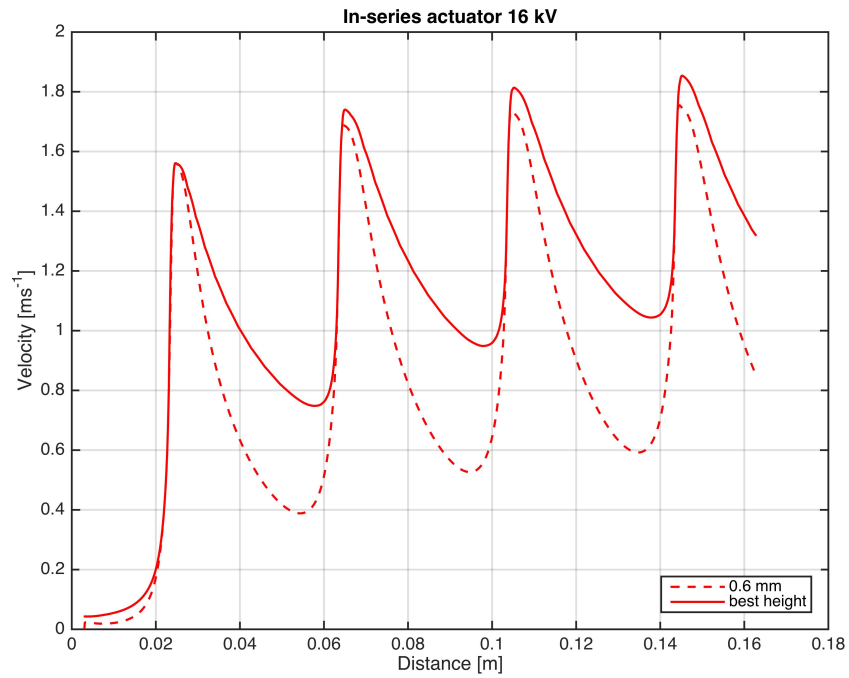
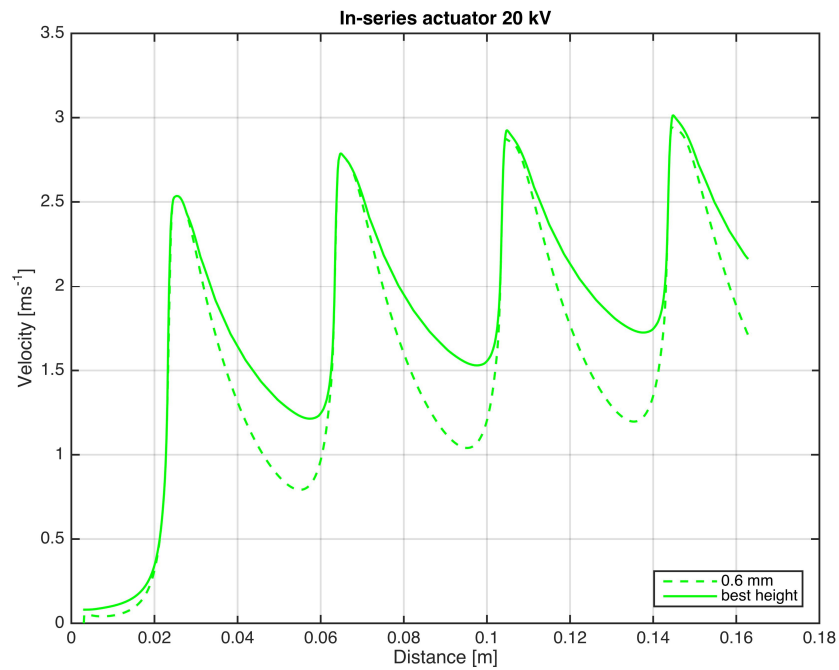**Figure 4.4:** Inline actuators for 16 kV, 1 kHz, 3 mm dielectric thickness at maximum height of 0.7769 mm

Figure 4.5: Inline actuators for 20 kV, 1 kHz, 3 mm dielectric thickness at maximum height of 0.6759 mm
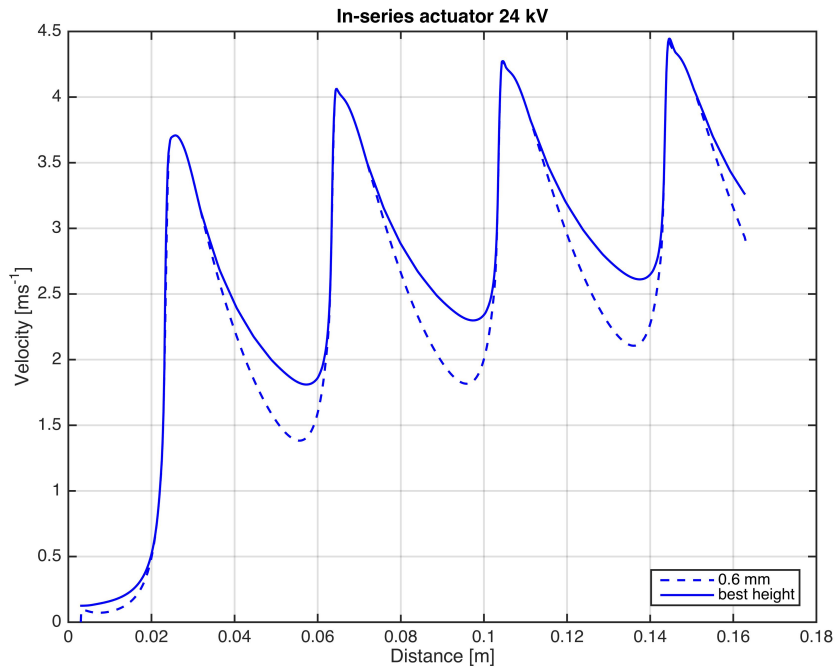
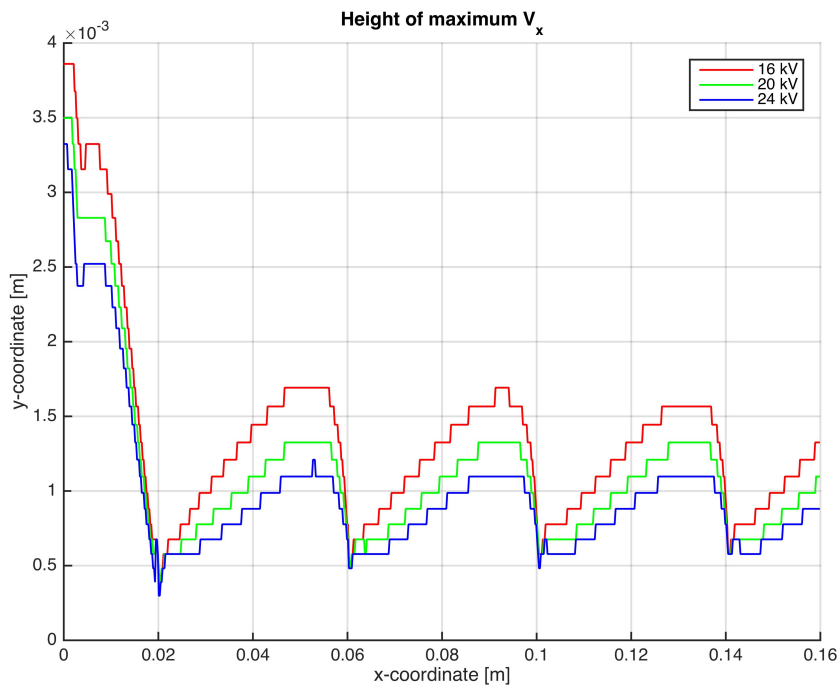**Figure 4.6:** Inline actuators for 24 kV, 1 kHz, 3 mm dielectric thickness at maximum height of 0.6759 mm

Figure 4.7: Height for maximum v_x in function of x coordinate

After these simulations, the sensitivity of the frequency on the actuators was as well studied. The same simulations as before were performed, with a different Soloviev's term for 5 kHz, shown in table 4.2. The applied force is around doubled for each actuator.

Voltage $[kV]$	Applied force [N/m]
16	0.016639
20	0.042131
24	0.089495

Table 4.2: Applied forces for 5kHz, 0.3075 cm dielectric thickness

The results are represented along with those obtained for the 1 kHz case. In figures 4.8, 4.9 and 4.10 the 5 kHz curve is shown in darker color. It is appreciated that the velocity is increased, with nearly the same trend along the four actuators. Other important fact is that, although the force applied by each actuator almost doubles, the maximum velocity does not, reducing the total efficiency of the actuators.
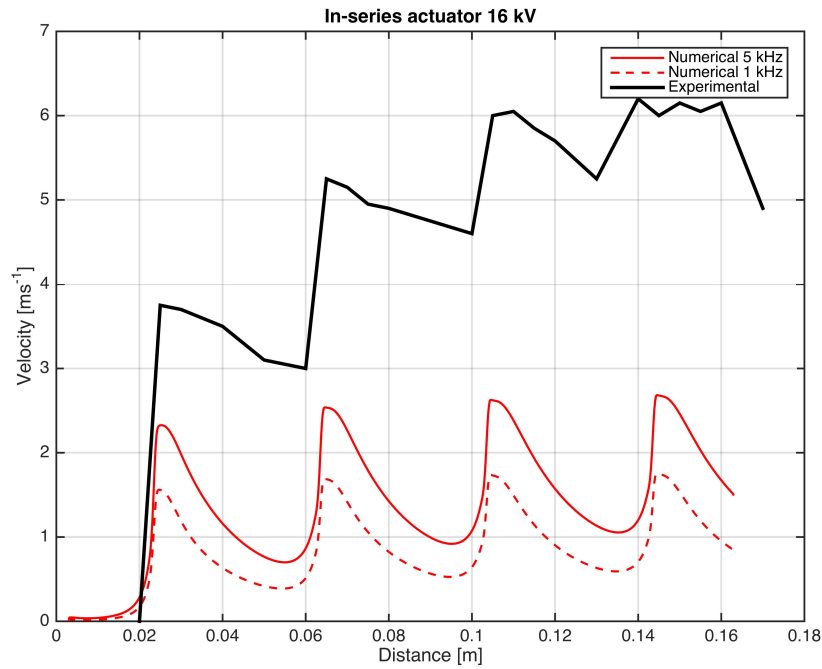

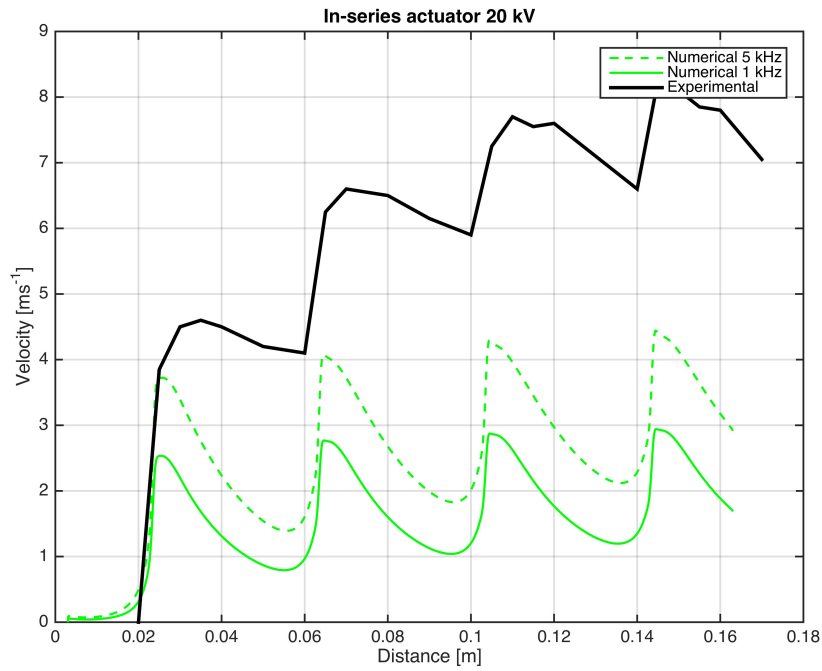**Figure 4.8:** Inline actuators for 16 kV, 5 kHz, 3 mm dielectric thickness

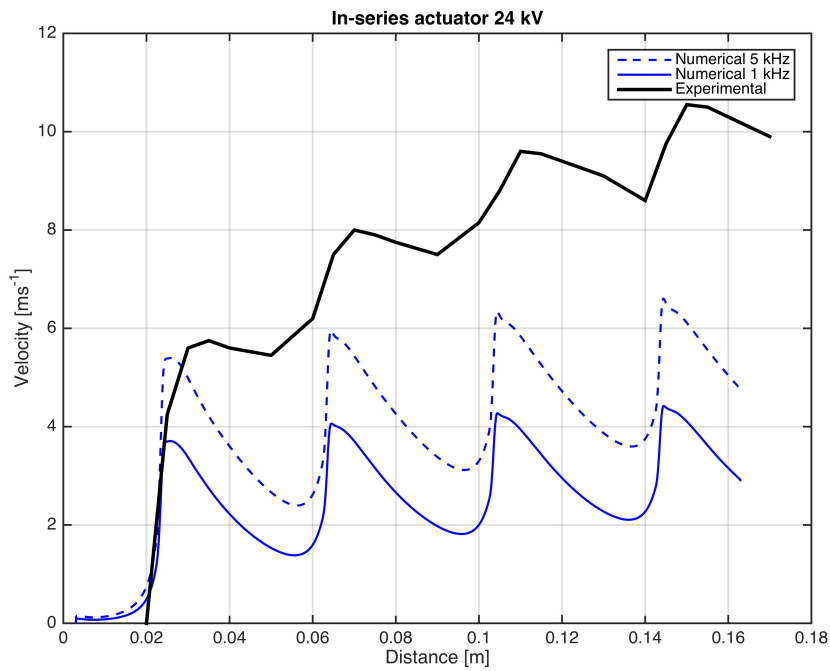**Figure 4.9:** Inline actuators for 20 kV, 5 kHz, 3 mm dielectric thickness

Figure 4.10: Inline actuators for 24 kV, 5 kHz, 3 mm dielectric thickness

Analyzing the velocity profile on the y axis at each actuator it is seen how the momentum is transferred to the upper layers of the fluid. Moreover, it is seen that the momentum is accumulated from one actuator to the front one, and by shear forces the air on top is accelerated. It is presented in figures 4.11, 4.12 and 4.13. This will be later important when studying the boundary layer control, as the momentum will behave in a similar manner.
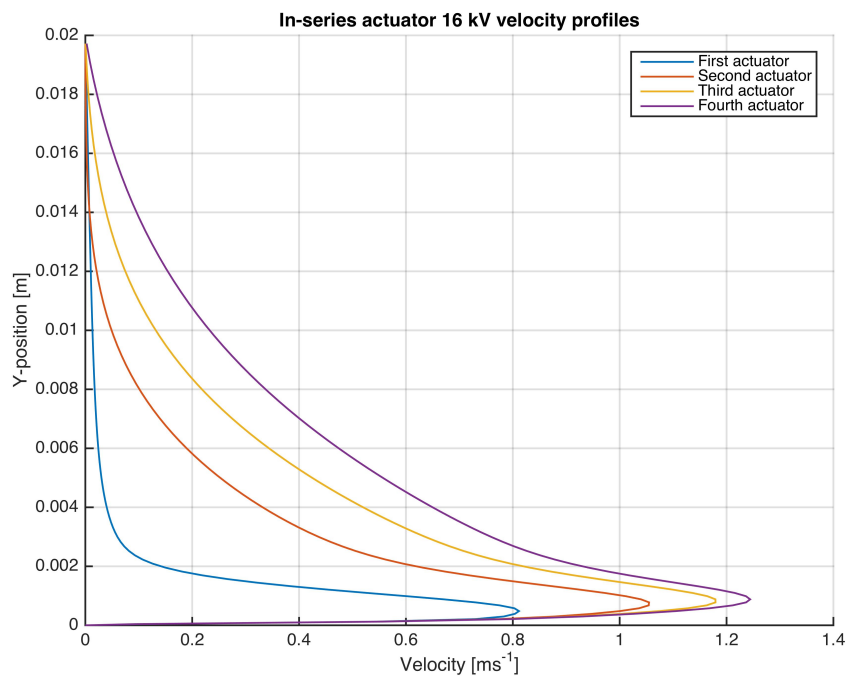

Figure 4.11: Velocity magnitude in function of altitude of the actuator, for location of each actuator. 16 kV
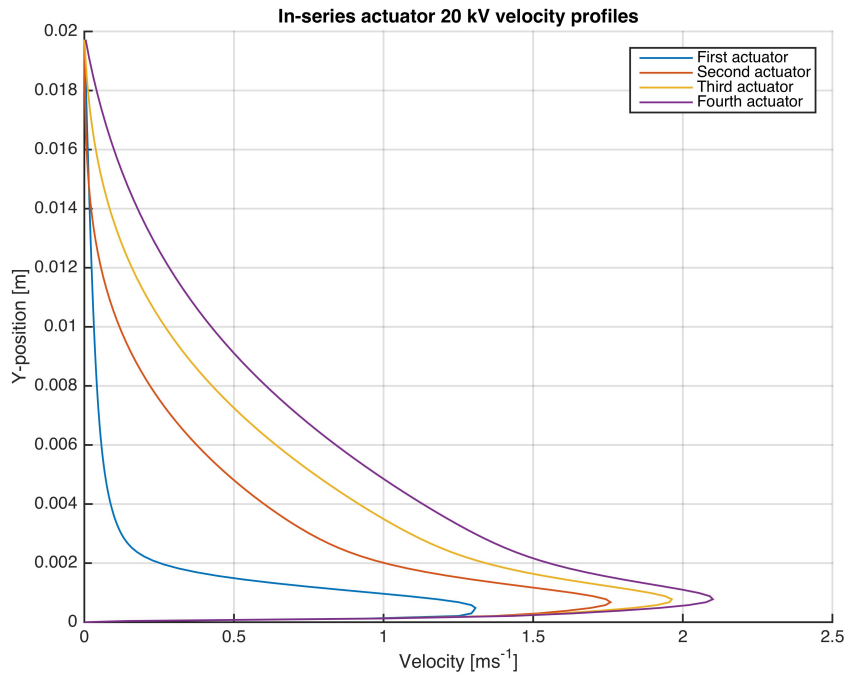
Figure 4.12: Velocity magnitude in function of altitude of the actuator, for location of each actuator. 20 kV
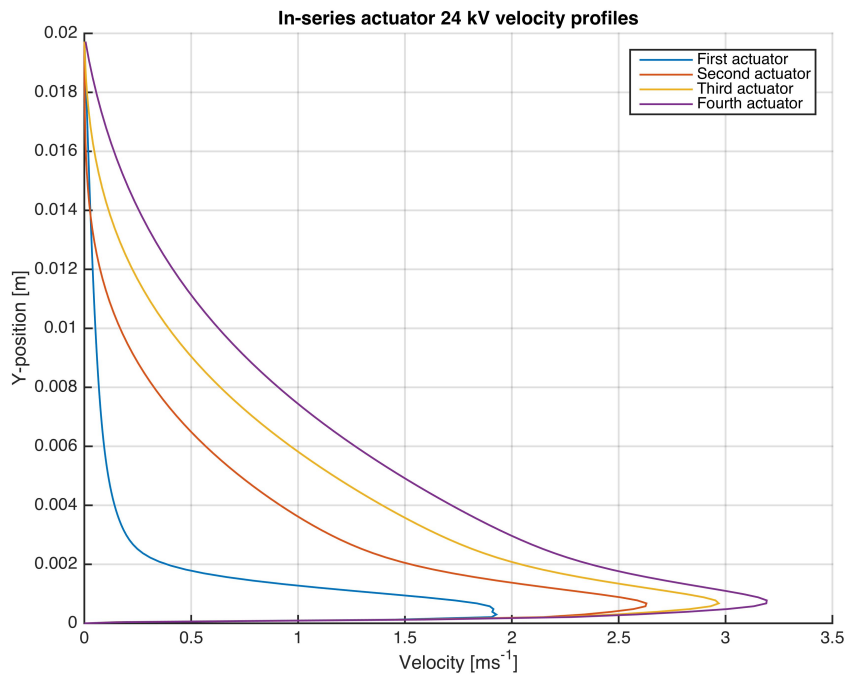

Figure 4.13: Velocity magnitude in function of altitude of the actuator, for location of each actuator. 24 kV

To conclude the analysis, a simulation with an arbitrary force of 0.15 N·m^{-1} as the Soloviev thrust was performed in order to reproduce the trend of the accumulation. This effect was not followed by the simulation, that compared to 24 kV case overshot the first value and did not reach the others. Moreover, the trend of the experiments was nearly as twice in slope as the numerical case.
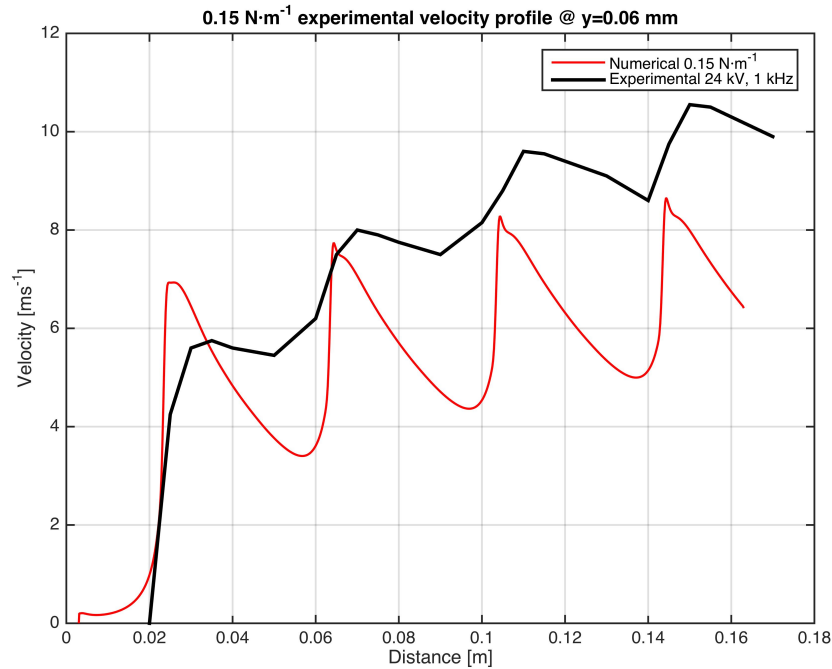

Figure 4.14: Generic 0.15 N·m^{-1} compared to 24 kV experimental data

The accumulation effect, therefore, is always present and can have a potential effect on future implementation. The main sources of error for miscalculations of the model come from inaccuracies of Soloviev's term, the distribution of the actuator's force and the shape of the actuator. The most accumulated velocity occurs for the first actuator in quiescent air. There is a dependency on the distribution of the actuator force, as more slender x-wise has a better momentum transfer and helps maintaining the velocity over a larger length, with less velocity decay and more improvement per stage. The actuator increases slightly its performance for large increases of the frequency, making it less efficient overall as more power is being consumed.

Application 2: Synthetic jet

5.1   Arrangement principle

In this chapter a more complex use of the DBD actuators is done. Two actuators have been placed in a flat plate facing one another. As studied by Bolitho and Barbato [3, 13], the effect is that of a synthetic jet that produces thrust. This vertical jet is generated by facing two air streams that scape towards the open volume. The shape and thrust produced by this model will be compared using the data from Barbato's experimental case.

Ilustrations in figure 5.1 show the principle of operation of both configurations, on the left for even thrust and on the right for uneven thrust. This jet can be vectored towards the sides by changing the parameters applied to each actuator (i.e., voltage and/or frequency) and hence the thrust (see figures 5.2). The results will be compared qualitatively to those obtained by Bolitho in [3], but using the configuration by Barbato explained hereafter.
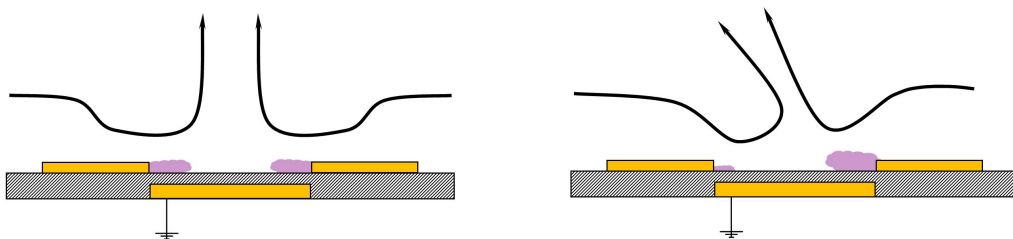

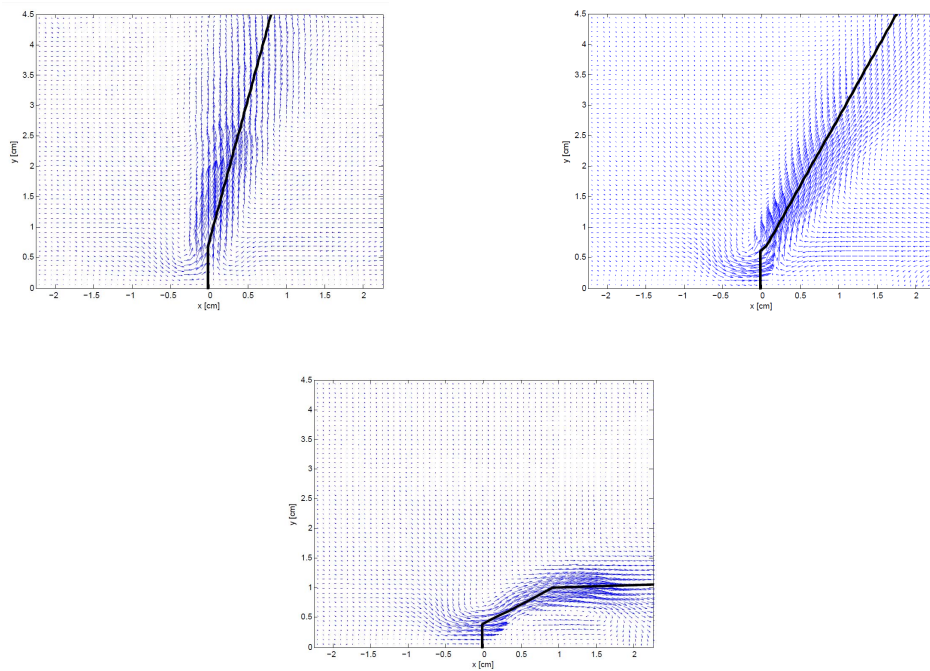**Figure 5.1:** Vertical jet actuator concept (taken from [3])

Figure 5.2: Experimental results for jet vectoring (taken from [3])

5.2   Geometry of the problem and parameters

This configuration is carried out in a control volume of 5×8 cm. The actuators were placed opposed one to each other. For this purpose, one of the actuators had to be rotated and the distribution replaced for a symmetric one. The actuators where placed at a distance of 10 and 16 mm each, corresponding to the length of the lower electrode and lower electrode gap, giving two configurations as set in Barbato's work. The thrust was calculated in accordance with the experiment parameters, substituting the terms in the model.

The mesh features an even configuration of 256000 elements, and the distribution among the sides was set so that these elements were square.

In the case of an asymmetrical thrust for the actuators, the mesh was biased to the bottom of the control volume to define better the resolution of uneven thrust. the bias factor was set to 7.5.

Each set of calculations converged at around 2×10^5 iterations at 1 second each. The variables studied were the thrust produced by the actuator and the shape of the jet.

The values studied range from 10 kV to 16 kV in steps of 2 kV. The only frequency studied was 6 kHz, due to the high computational times involved. The applied voltages with its corresponding thrust are shown in table 5.1.

Voltage $[kV]$	Applied force [N/m]
10	$7.2588 \cdot 10^{-3}$
12	0.015821
14	0.030363
16	0.052174

Table 5.1: Applied forces for 6 kHz, 0.1 cm dielectric thickness

In the case of the jet vectoring, the values used were varied for the right actuator to the values presented in 5.2. They will be later presented in terms of the ratio of right actuator with respect to the left actuator.

Voltage $[kV]$	Applied force [N/m]
13	0.021371
11.9	0.017623
11.35	0.012012
10.8	$9.7163 \cdot 10^{-3}$
9.15	$4.760406 \cdot 10^{-3}$

Table 5.2: Applied forces for 5 kHz, 0.1 cm dielectric thickness, uneven thrust

5.3 Vertical jet results and analysis

The first parameter to be studied is the shape of the actuator and compare it to the experimental results. For this, a 12 kV, 0 mm gap separation has been plotted in the velocity contour map, figure 5.3. It is compared to the images obtained by Barbato on [13], obtained by Schlieren photography, where the shape and upper diffusion coincides.

For the case of 0 mm gap, it was observed that a recirculation zone ocurred in the intersection of the actuators close to the wall, and it extended into the lower part of the actuator for some cases (figure 5.4). This produced shallow inclinations of the jet, despite the fact that the simulations showed convergence. This behavior was not observed when the actuators where separated by 3 mm. Therefore, a priori the gap has an effect on the morphology of the jet.

Barbato studied as well the thrust produced by the actuator. To compare the results, the vertical force produced by the jets on the aforementioned configuration
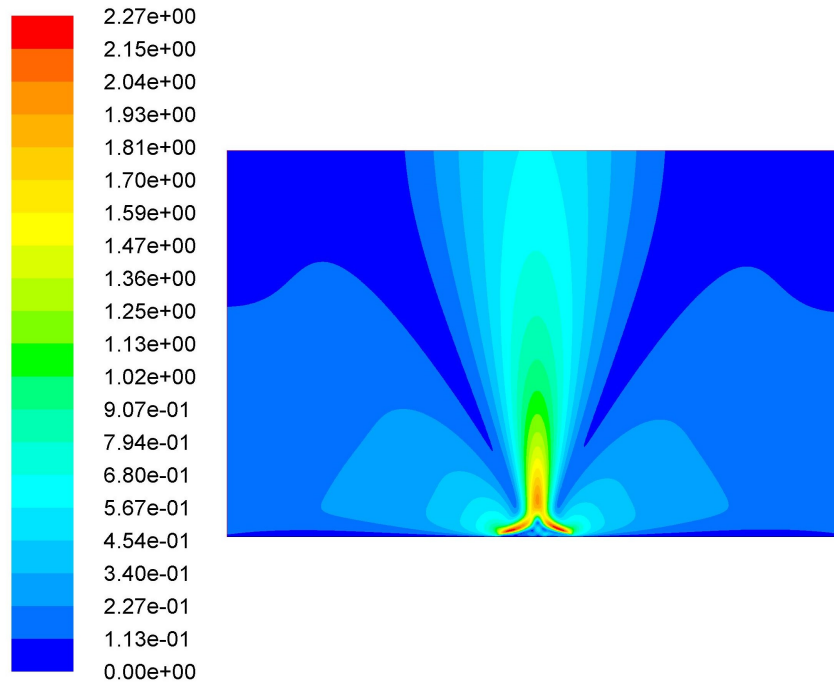
Figure 5.3: Velocity contour map in m·s^{-1} of 12 kV, 0 mm gap, 6 kHz opposed actuators.
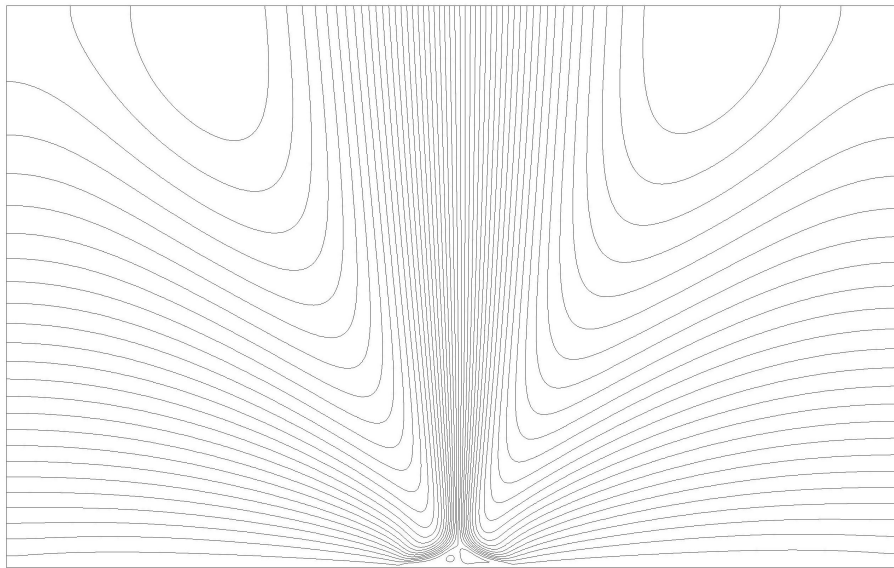

Figure 5.4: Streamlines for vertical actuator. Note the recirculation zone below the jet.

was extracted in function of the length of the actuator. Multiplying by the length of Barbato's actuator (0.07 m), the numerical force is obtained. In figure 5.5 the experimental and numerical solutions are presented.
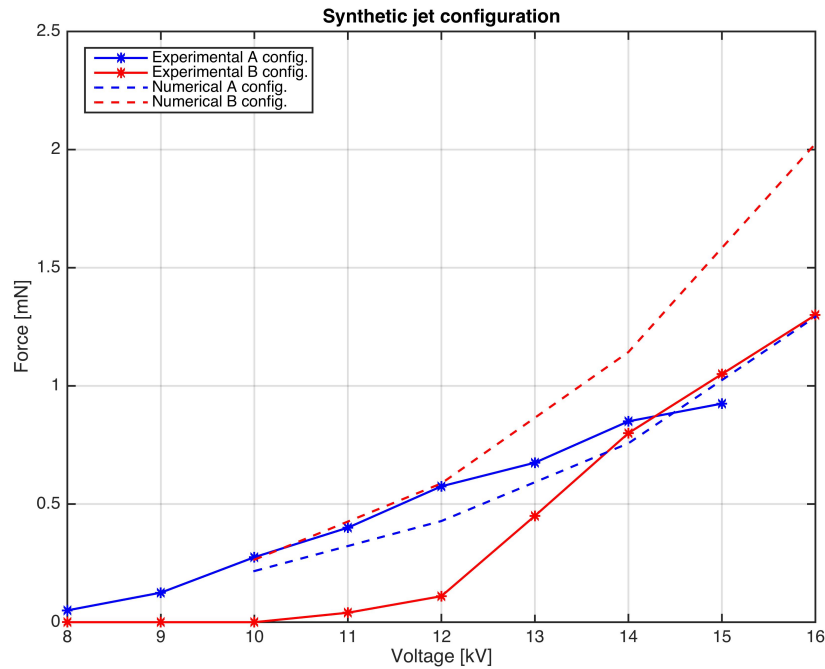
Figure 5.5: Force for A (0 mm) and B (3 mm) configurations, experimental in blue and numerical in red.

It is seen that the numerical curves show an exponential shape, while the experimental curves tend to be exponential for low values of voltage and linear until limit of current. This is due to the fact that, for higher values, the actuator experiments a saturation effect before arching. Despite this fact, the trends followed before this arching are compliant with the numerical results, although the data has a mismatch. This mismatch can be due to the slight error from the Soloviev term, while for case B the distribution of the force may impose greater discrepancies, as no recirculation occurred in the intersection, and no overlaping of the actuators occured as well.

Figure 5.6 shows the y component of the velocity in the symmetry plane. The maximum velocity at this point is achieved by the 0 mm actuators, while it is more distributed for 3 mm actuators. Moreover, there is more momentum transfer for the later, providing more movement of air and performing better thrust than 0 mm actuators with the same force. It is of interest 14 kV, 0 mm case, where the velocities in this plane were slower than the analogous 0 mm case.
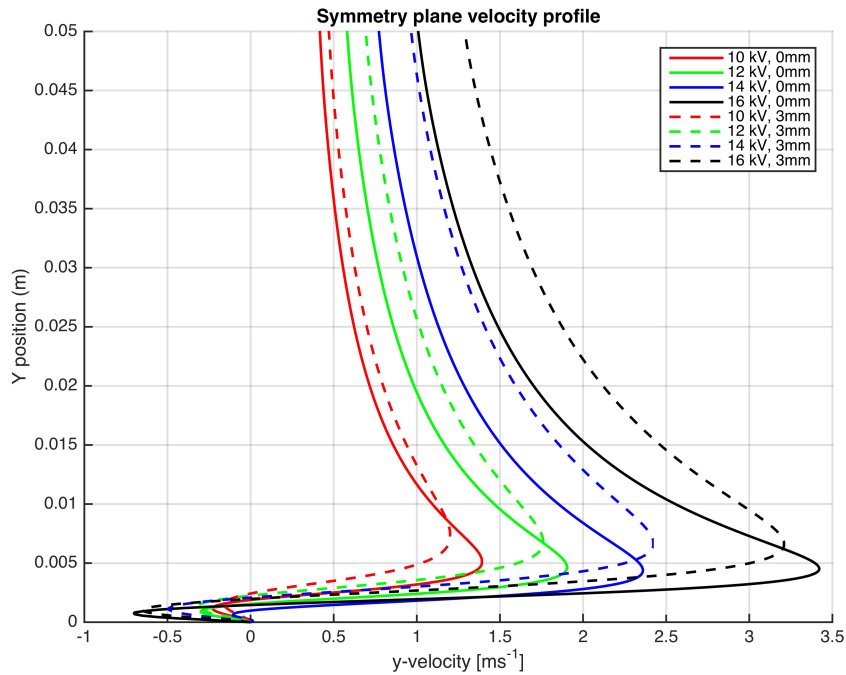
Figure 5.6: Velocity contour map for all actuators at symmetry plane for different configurations.

Analyzing this in detail, it was discovered that a slight tilting occurred (figure 5.7), meaning that the jet was not completely vertical. This was caused by small recirculations below the actuators, even when the cases were recomputed. This did not affect the force produced by the actuator.
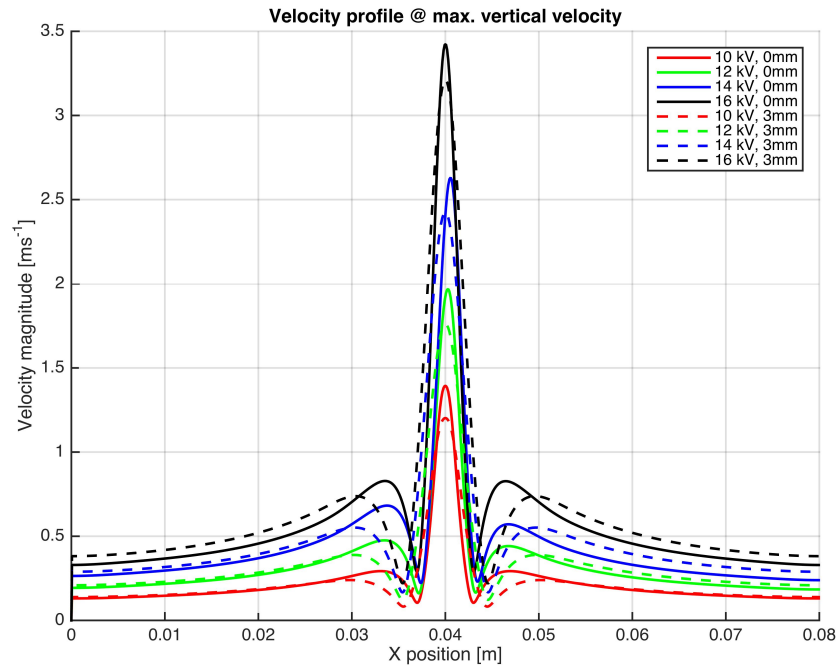
Figure 5.7: Velocity magnitude for all actuators at maximum vertical velocity height.

Regarding the height where maximum vertical velocity takes place, the v_x and v_y velocity profiles (figures 5.8 and 5.9) it is seen that the actuator forces the air from the surroundings more evenly for the case of gapped electrode. This has an important effect on the effectiveness of the actuator, as more mass of air is being moved with lower peak velocity of the jet, increasing the effectiveness of the applied energy on the fluid.
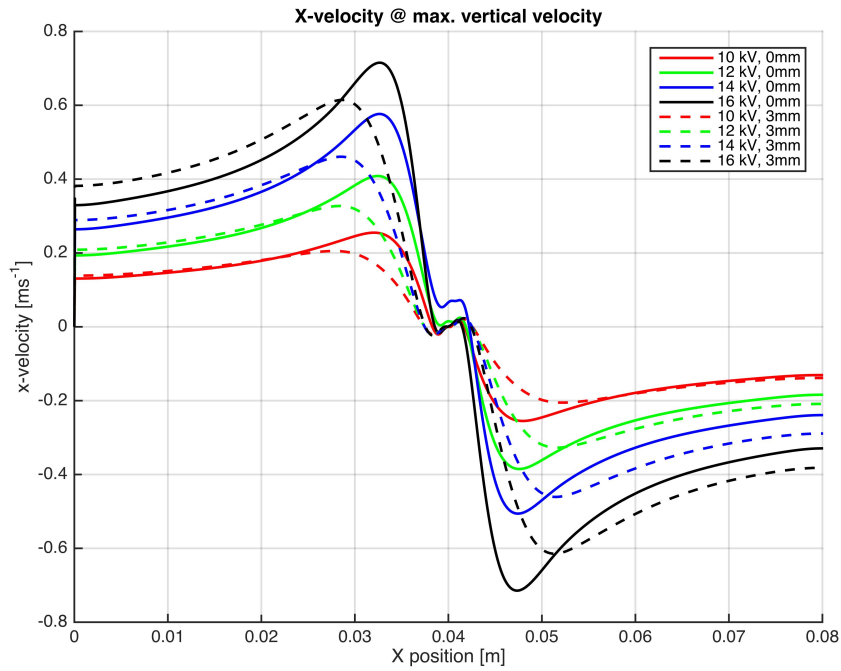
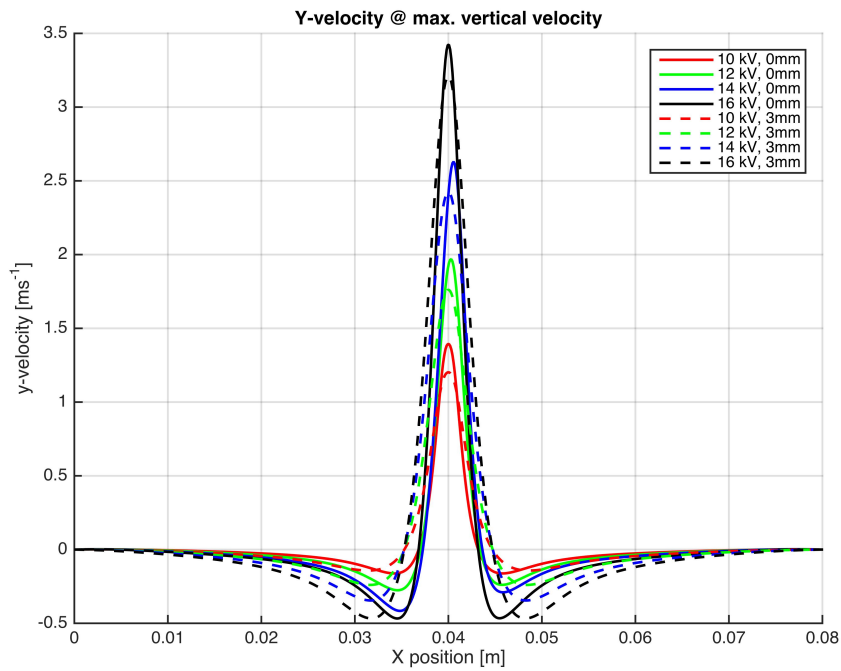**Figure 5.8:** X-velocity for all actuators at maximum vertical velocity height.

Figure 5.9: Y-velocity for all actuators at maximum vertical velocity height.

As the y-coordinate increases, so does the y component of the air next to the symmetry axis, shown in figures 5.12 and 5.15. This velocity is transferred by shear forces towards the sides, and there is a point where the air is no longer sucked in thestream but the jet diffuses. This is shown in figures 5.11 and 5.14, where the velocity goes outwards instead of inwards. This is also shown in Barbato's figures, where the jet diffuses.
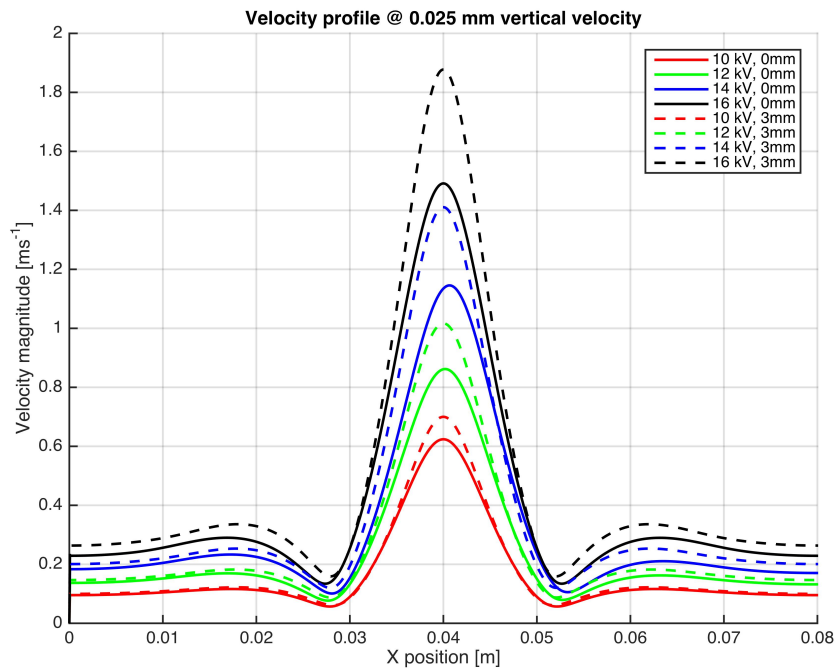

Figure 5.10: Velocity magnitude for all actuators at 0.025 mm height.
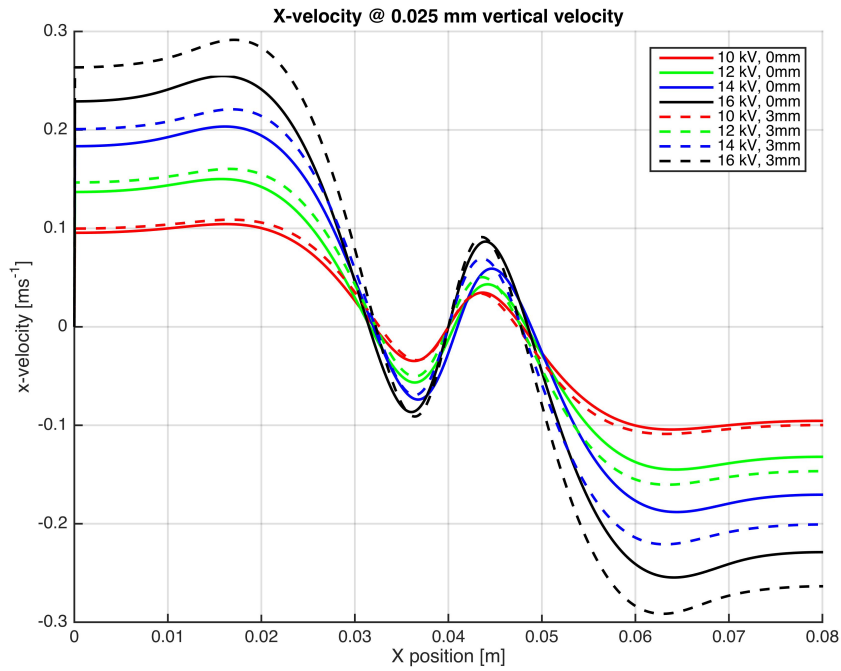
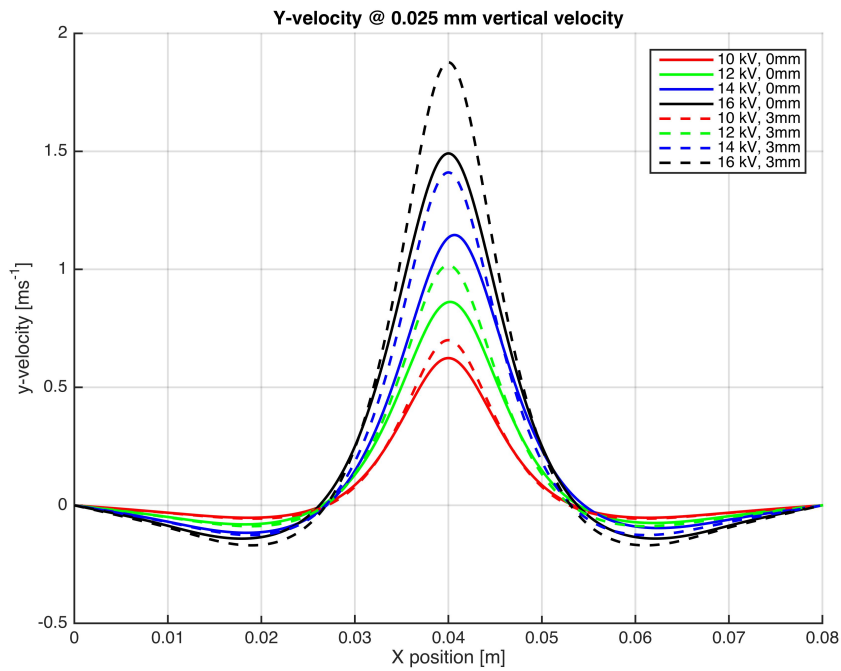**Figure 5.11:** X-velocity for all actuators at 0.025 mm height.

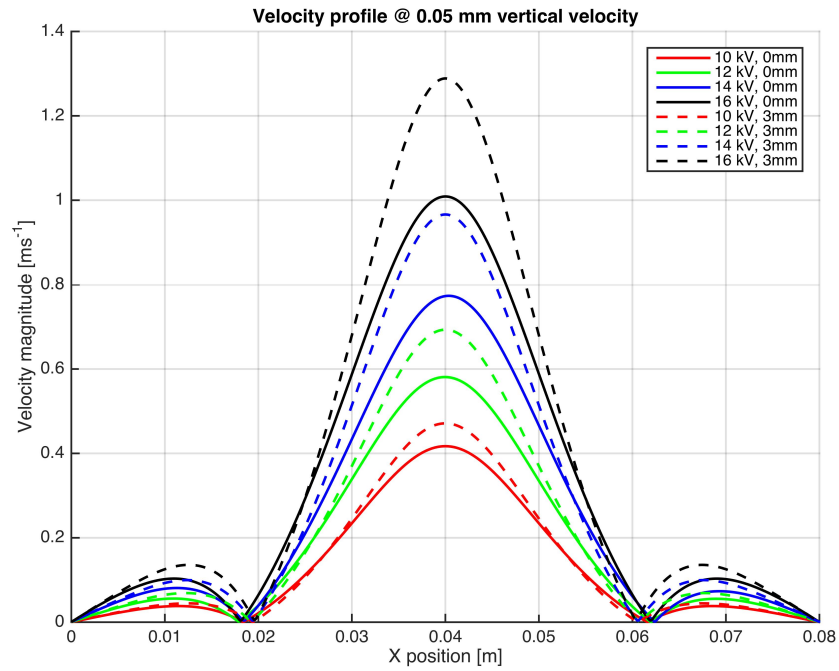**Figure 5.12:** Y-velocity for all actuators at 0.025 mm height.

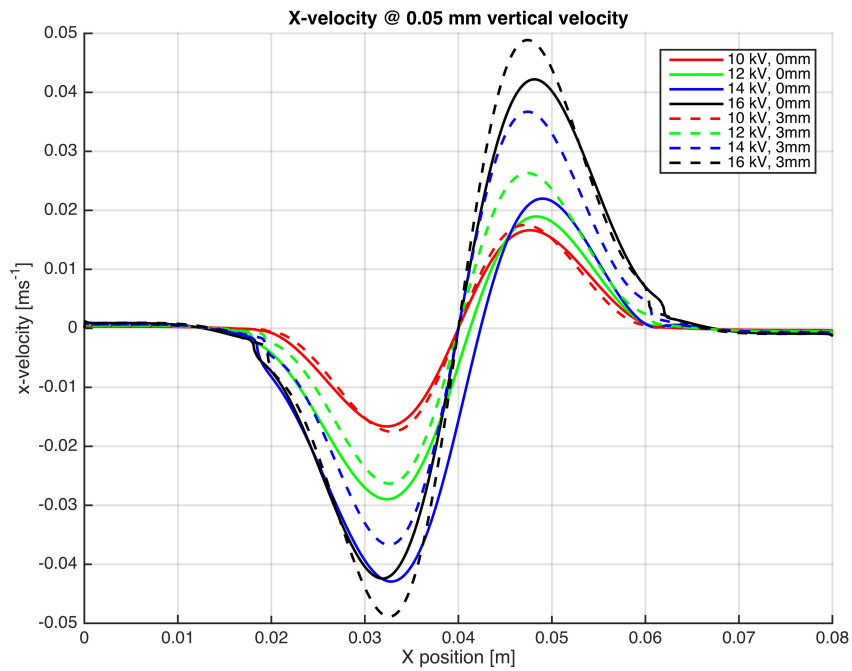**Figure 5.13:** Velocity magnitude for all actuators at 0.050 mm height.

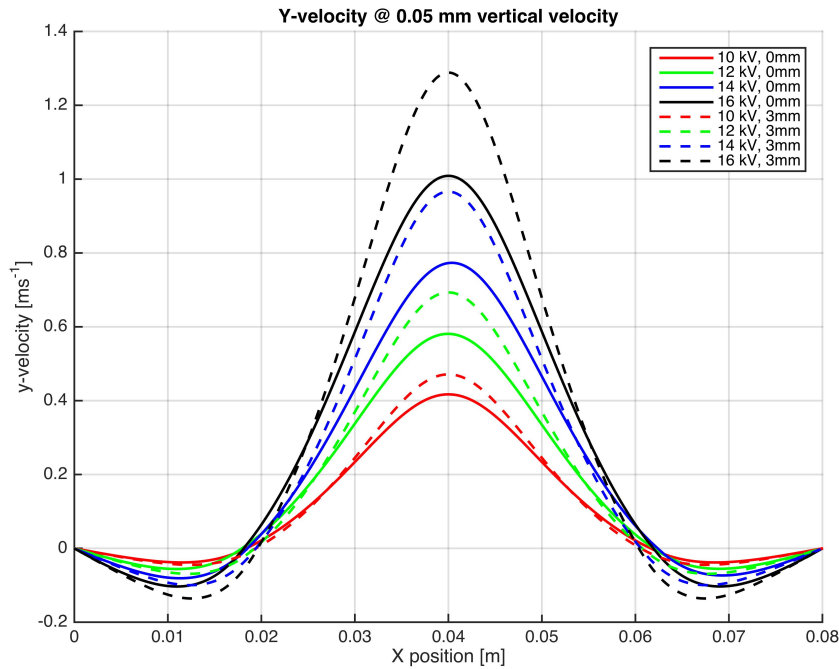**Figure 5.14:** X-velocity for all actuators at 0.050 mm height.

Figure 5.15: Y-velocity for all actuators at 0.050 mm height.

5.4   Jet vectoring results and analysis

Varying the applied voltage to one of the actuators results in a decreased induced velocity by that actuator, having as an effect a tilting of the direction the jet is directed. To analyze this angle, the maximum y-velocity height was found for each of the aforementioned cases, and the angle of the velocity plotted in function of the x coordinate (figure 5.17). The desired angle of the jet corresponds to that of the axis of the jet. In the vicinity of this axis, the jet slightly diffuses, meaning that the angle tends to vary clockwise in function of x. However, further from the jet, the air is being dragged by the jet itself, producing a change in the vector angle counterclockwise in function of x coordinate. Therefore, the inflection point at a given altitude marks the axis of the jet, and therefore the angle.

In figure 5.17 the angles for the best height have been plotted, and the resulting value is presented in figure 5.3.

Voltage right actuator[kV]	Angle [degrees]
11.9	80.76
11.35	65.53
10.8	48.30
9.15	3.221

Table 5.3: Applied forces and resulting angles for vectoring applications from the horizontal.
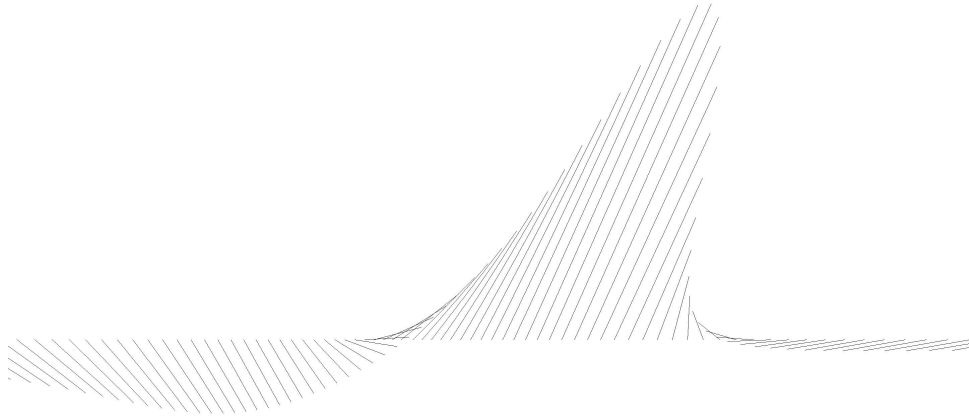

Figure 5.16: Vectors at maximum vertical velocity height.

Regarding the behavior of the jet, the velocity vectors are shown in figures 5.18, 5.19, 5.20 and 5.21. It is seen that the main contribution to the jet velocity comes from the strongest actuator, while the limited actuator serves to the purpose of lifting the air and producing the jet towards that direction.
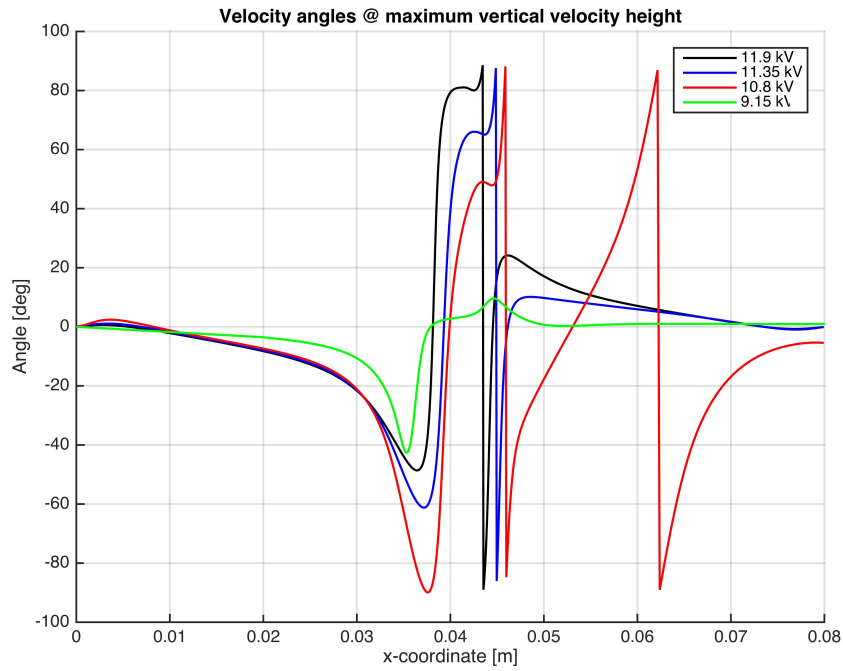
Figure 5.17: Velocity angle with respect to the horizontal for maximum v_y height. Discontinuities represent third and fourth quadrant angles.

Figure 5.18: Velocity magnitude contours [m·s^{-1}] for $\frac{T}{T_0}$=0.8246 right actuator.

Figure 5.19: Velocity magnitude contours [m·s^{-1}] for $\frac{T}{T_0}$=0.56207 right actuator.
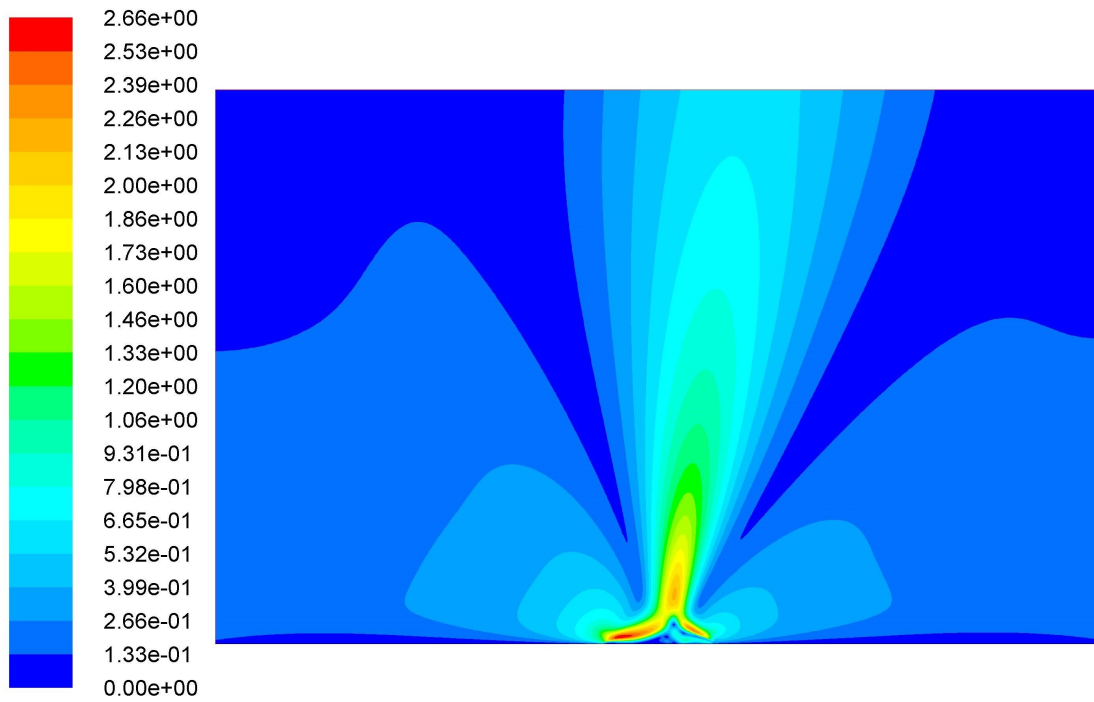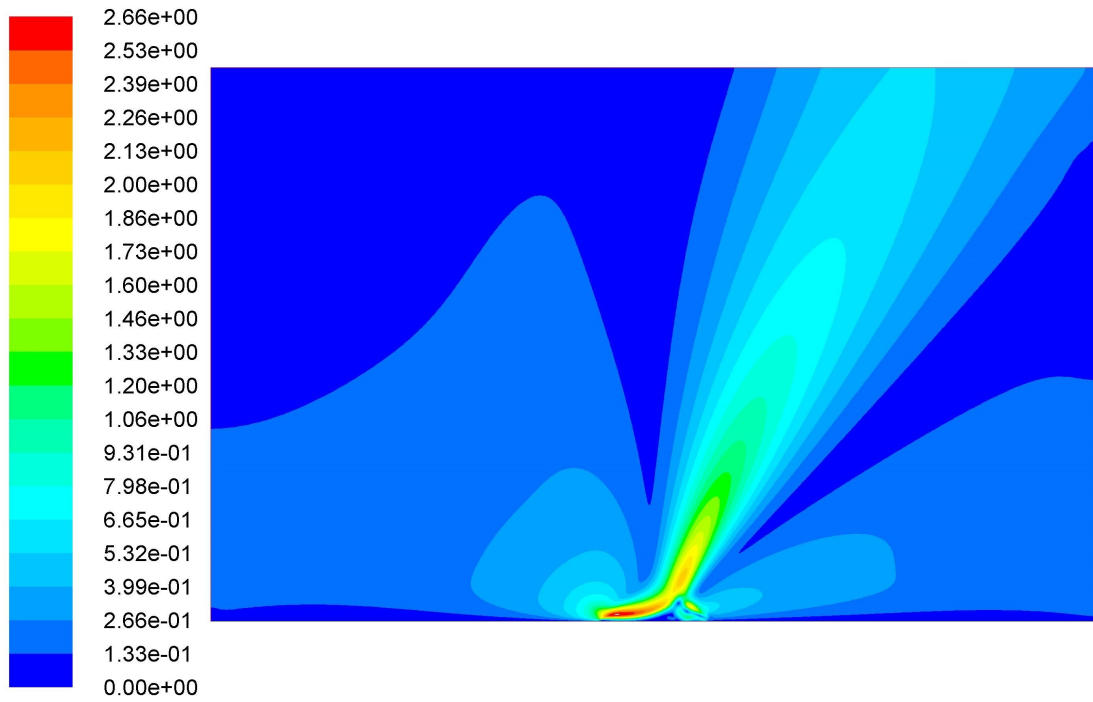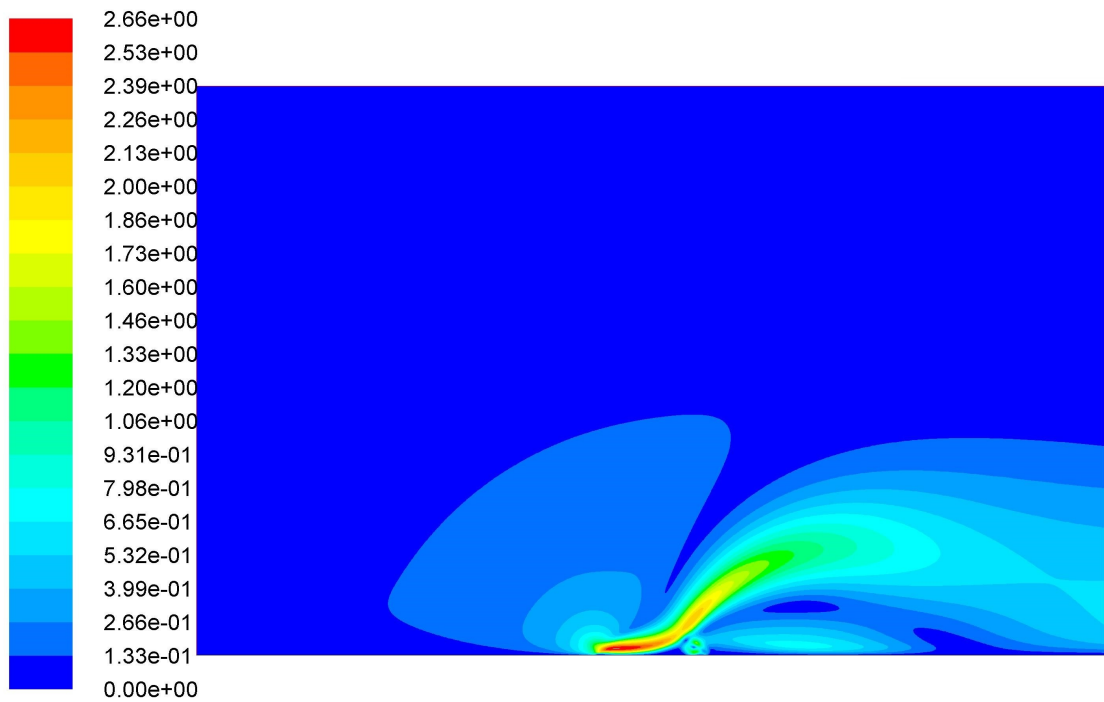

Figure 5.20: Velocity magnitude contours [m·s^{-1}] for $\frac{T}{T_0}$=0.454648 right actuator.
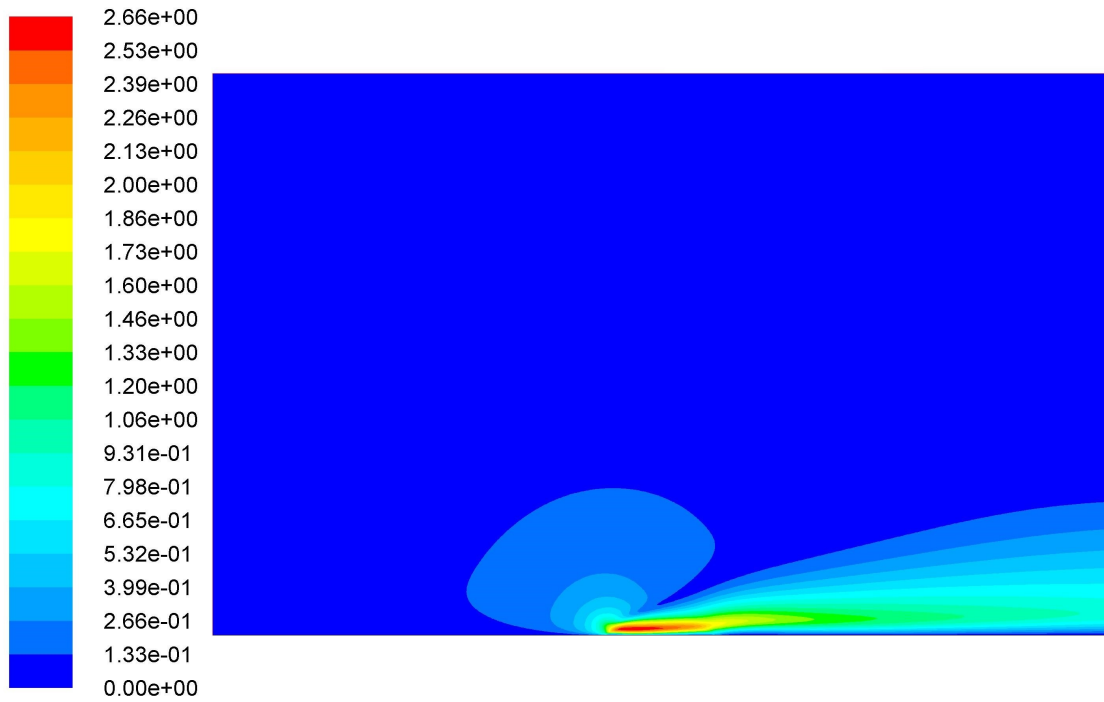
Figure 5.21: Velocity magnitude contours [m·s^{-1}] for $\frac{T}{T_0}$=0.222750 right actuator.

It is seen in figures 5.22, 5.23, 5.24 and 5.25 that, for 45° or smaller, the jet is not anymore straight and tends to attach to the surface. This is explained by the fact that, differently from a normal air jet, the air propulsed comes from the surroundings. Therefore, if the jet tilts too much, the air of the jet is recirculated towards the actuator. This was as well regarded in the velocity angles of the previous image, as the angles oscillate a full revolution. This is compliant with the results obtained by Bolitho in previous figure 5.2, where the recirculation is also present for more extreme values of the angle.
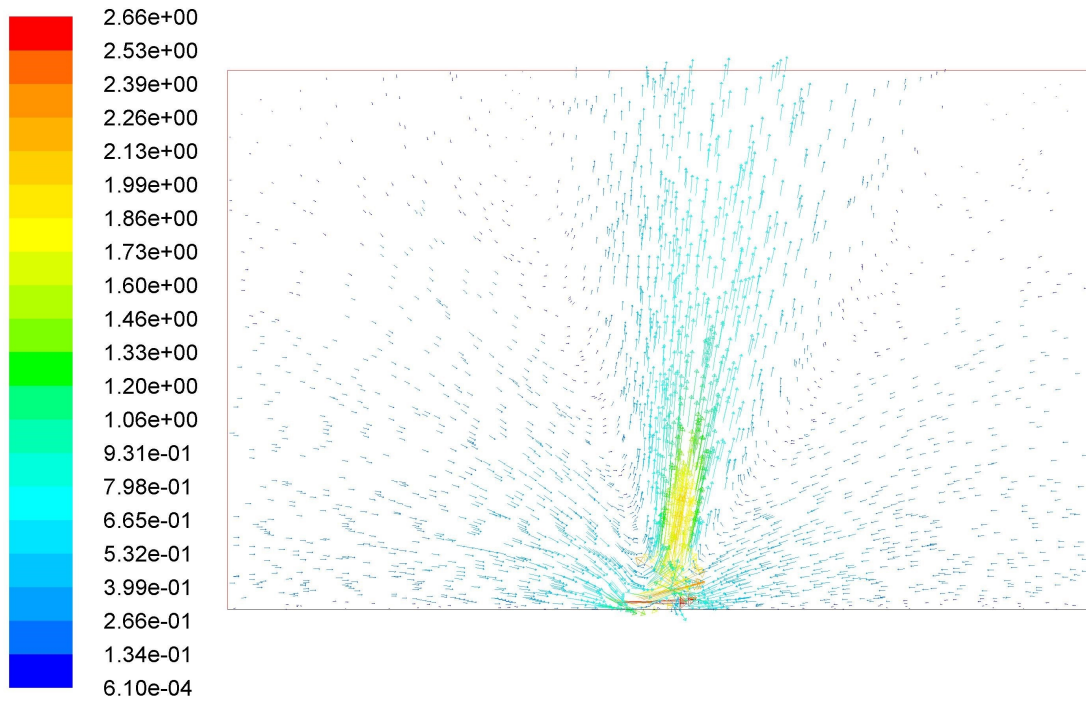
Figure 5.22: Velocity magnitude [m·s^{-1}] for $\frac{T}{T_0}$=0.8246 right actuator.
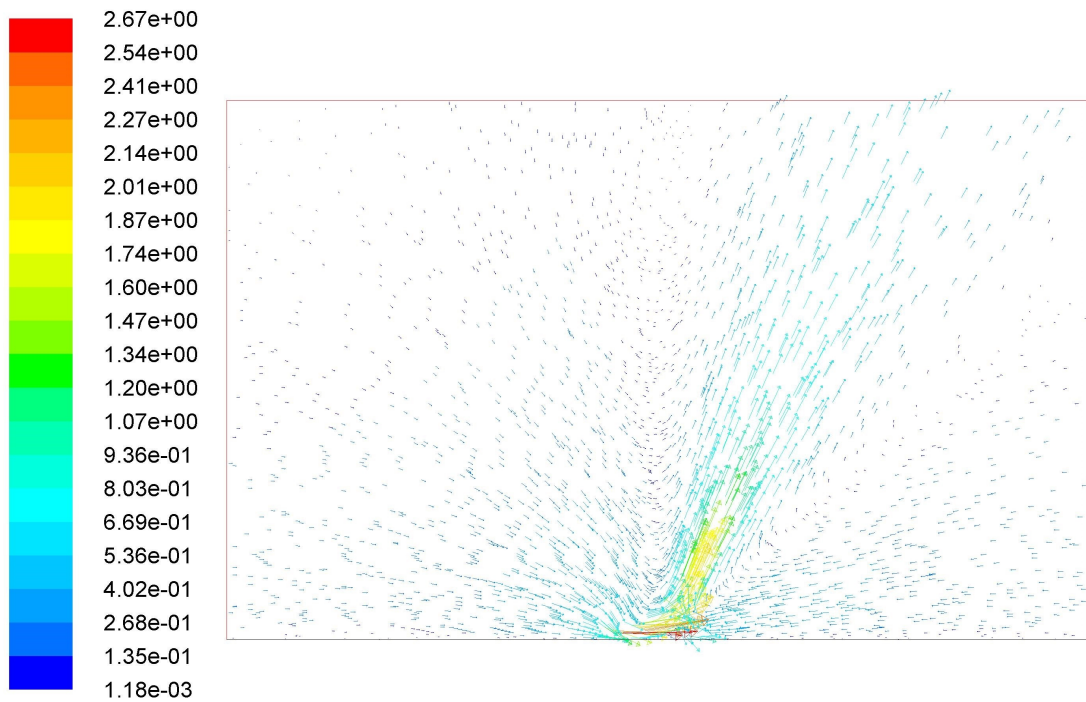
Figure 5.23: Velocity magnitude [m·s^{-1}] for $\frac{T}{T_0}$=0.56207 right actuator.

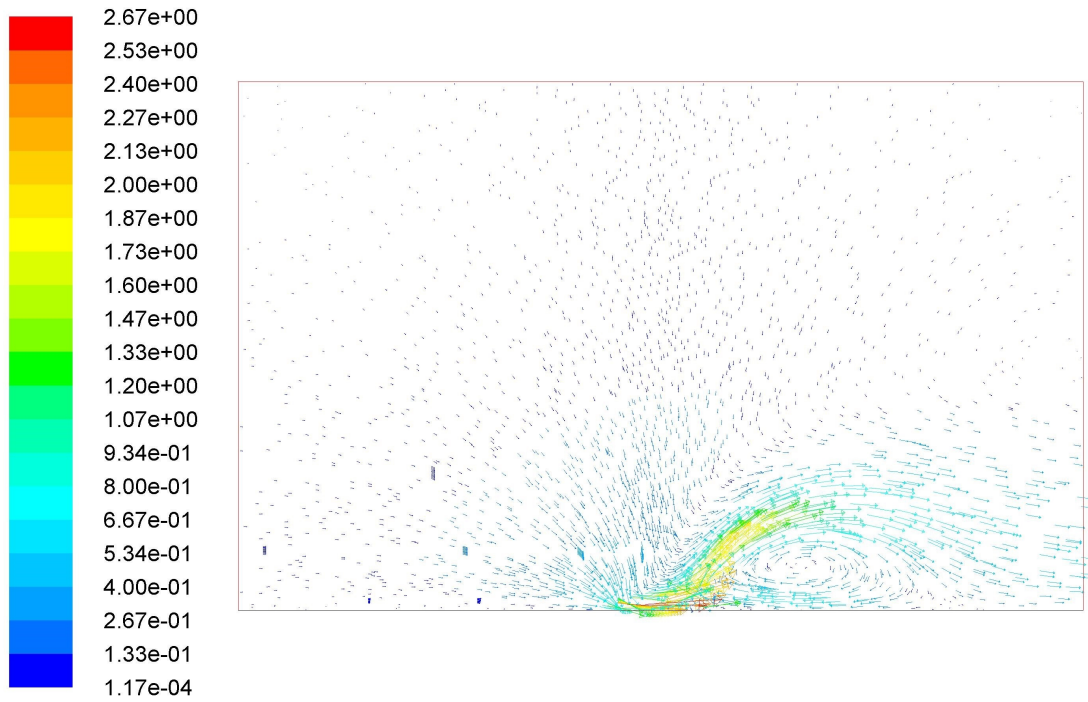**Figure 5.24:** Velocity magnitude [m·s^{-1}] for $\frac{T}{T_0}$=0.454648 right actuator.

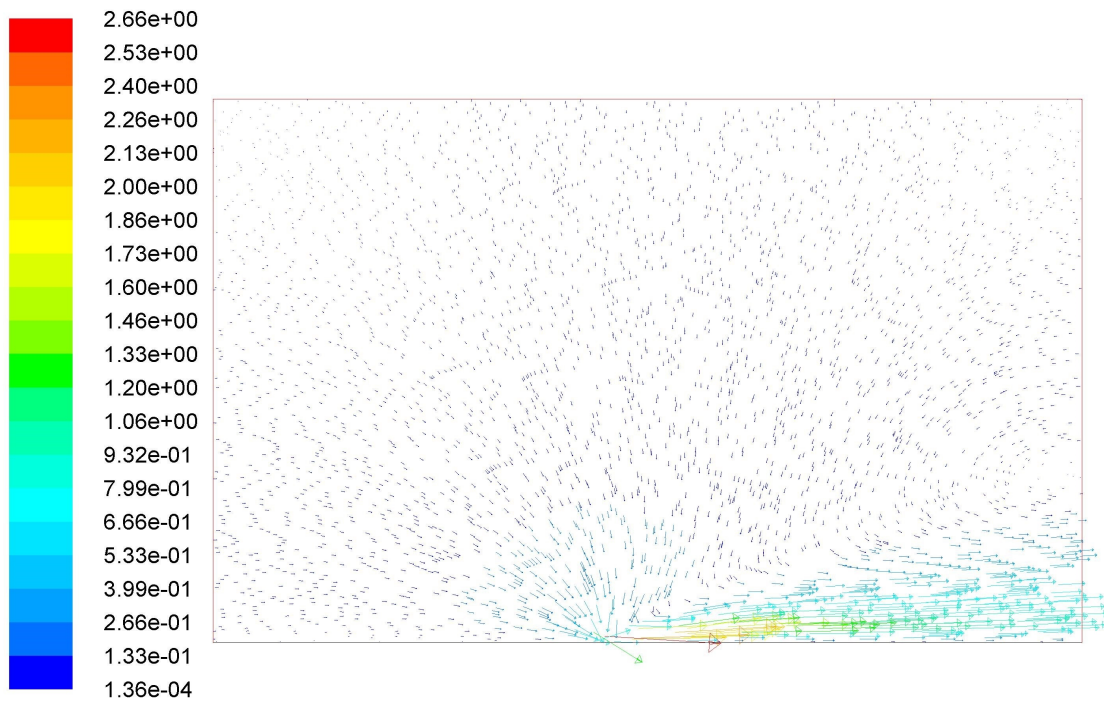**Figure 5.25:** Velocity magnitude [m·s^{-1}] for $\frac{T}{T_0}$=0.22275 right actuator.

The effect of a synthetic jet has been proven for opposing actuators, as well as the jet vectoring, providing close results to those obtained in experiments. There is a strong dependency of the distance of the actuators on the performance, and an optimization has to be done in order to select the most appropiate distance for efficiency. The separation has as well an effect of a recirculation zone in the intersecting points of the actuator, and for the closest arrangement recirculation may appear below the actuator, creating instabilities. It is more efficient to generate the thrust by moving more air from the surrounding than producing a high peak velocity, which is tweaked by gap separation.

In the case of jet vectoring, it has been shown that for different values of voltage drop the jet effectively changes inclination up to a valid point. This point shows good agreement with the experimental results in terms of shape of and effects of the actuators, not so for the angles at which it occurs. The jet is deviated at high vectoring angles due to recirculation near the actuator being limited, deviating it until it is horizontal. The most contribution to the moment of the actuator comes from the strong one, while the other serves as an opposing force that lets the jet rise to a desired angle.

Application 3: Airfoil actuators

6.1   Arragement principle

In this chapter an implementation of an arrangement of actuators over an airfoil will be studied.

Experiments using DBD actuators on airfoils have been extensively investigated from experimental and computational [6, 16, 17, 18] point of view. In this kind of application, the DBD actuators are used to promote reattachment of the fluid onto the airfoil's surface when stall is expected. An early experimental work demonstrating the potential of DBD actuators to mitigate separation flows is documented in [4]. The observable effect is depicted in figure 6.1, where in the left and right are shown respectively the flow over the airfoil when plasma actuators are powered off and on.

In the following, a NACA symmetric airfoil will be used to assess the potential of the model in a low Reynolds number configuration.
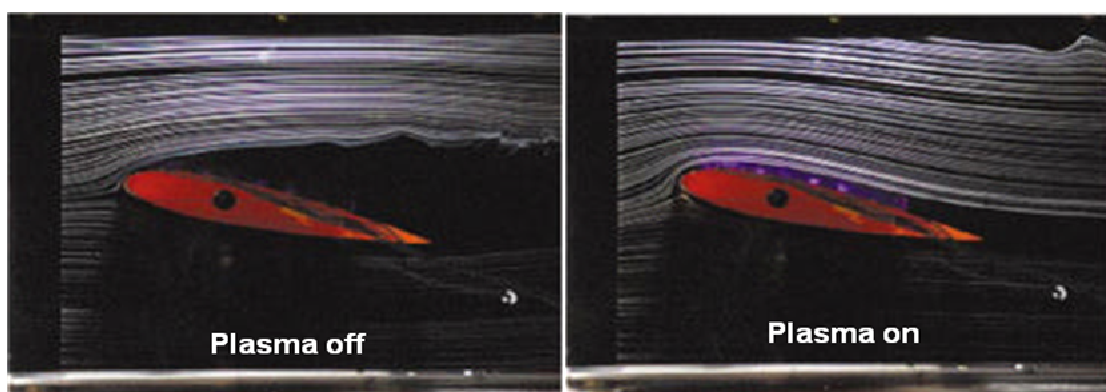

Figure 6.1: Reattachment of separated flow with actuator off and on for NACA 0015 Airfoil at $\alpha = 12°$, flow velocity 2.6m·s^{-1} (Smoke used for visualization) as in [4]

6.2   Geometry of the problem and parameters

The profile used is a NACA 0010 symmetric profile with a chord of 0.1 m. The model was generated by a Matlab code with the thickness distribution formula, and 200 points with even distribution in the x direction were calculated. The model was later integrated in Fluent.
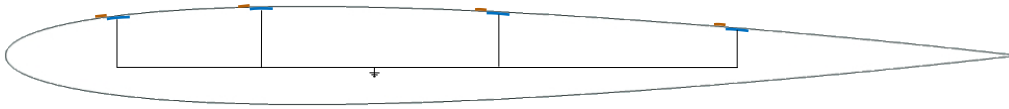

Figure 6.2: Sketch showing the arrangement of actuators. Locations in function of the chord are 0.1c, 0.25c, 0.5c and 0.75c

The simulating volume used was a semicircle spanning from the trailing edge with a radius of 0.2 m, with a box mesh downstream of 0.2×0.4 m. The mesh is composed by 120000 elements, with greater concentration at leading and trailing edges, as well as the downstream direction of the chord. This was refined for better definition of the actuator near the wall, and to avoid high aspect ratios of cells that produced numerical instabilities. The boundary conditions were set to velocity-inlet, to simulate a flow of 8 m·s^{-1} with a 16° of angle of attack, the airfoil as a wall (for non-slip condition) and the other boundaries as pressure-outlet.

The simulations were run first without any actuator, then with one actuator at 0.25c. As the bubble was reduced but not eliminated, another actuator was placed at 0.75c. Later simulations included others at 0.5c and 0.1c. All the actuators were placed with a generic force of 0.1 N·m^{-1} and flat to the surface. This means that the derivative of the thickness function with respect to the x directon was calculated, and the value used to obtain the inclination angle. This angle was used implemented on the UDF to account for the rotated force of the actuator. The values of the angles are presented in table 6.1

Position [m]	Rotation angle [degrees]
0.1c	-8.005
0.25c	-1.2048
0.5c	3.011
0.75c	4.958

Table 6.1: Rotation angles for each actuator. Positive angles are referenced from the horizontal clockwise as explained in chapter 3

6.3   Results and Analysis

The first calculation considered was over a clean airfoil with an angle of attack of 16°. The streamlines show clear separation of the fluid from the leading edge to the trailing edge, with recirculation behind the airfoil. The stagnation point is seen at the leading edge of the airfoil, below it. Moreover, it is seen that the fluid is detached at the back, and Kutta condition is not held.
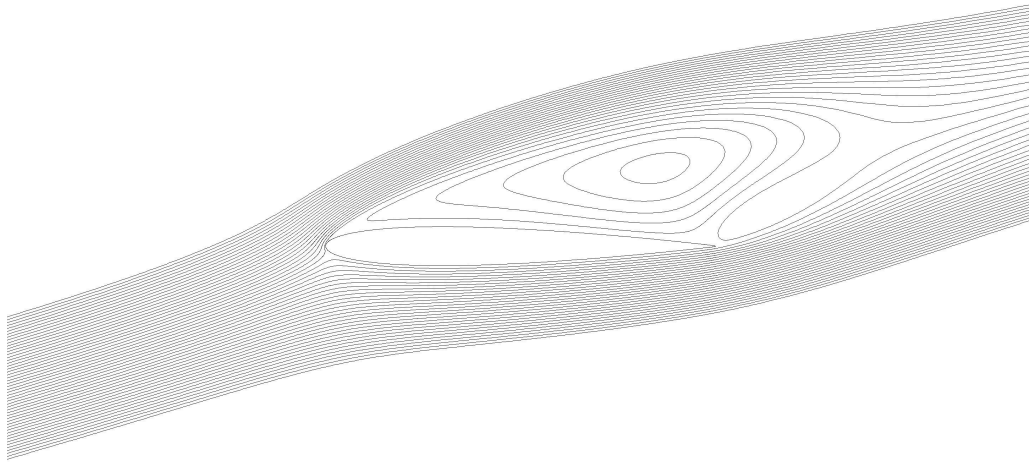

Figure 6.3: Streamlines for no actuator on.

However, when an actuator is on, the recirculation diminishes and becomes smaller. This is seen in figure 6.4, where the recirculation zone is broken into two smaller recirculation zones. The same happens with two actuators placed on the surface of the wing, which further diminishes the bubble (figure 6.4).
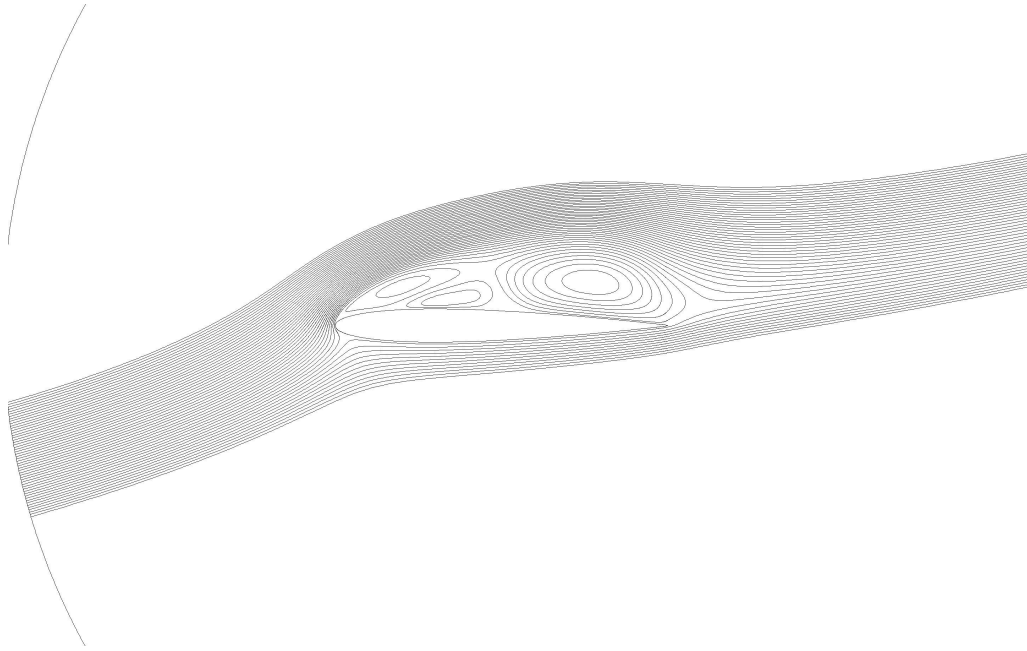
Figure 6.4: Streamlines for 0.25c actuator on.
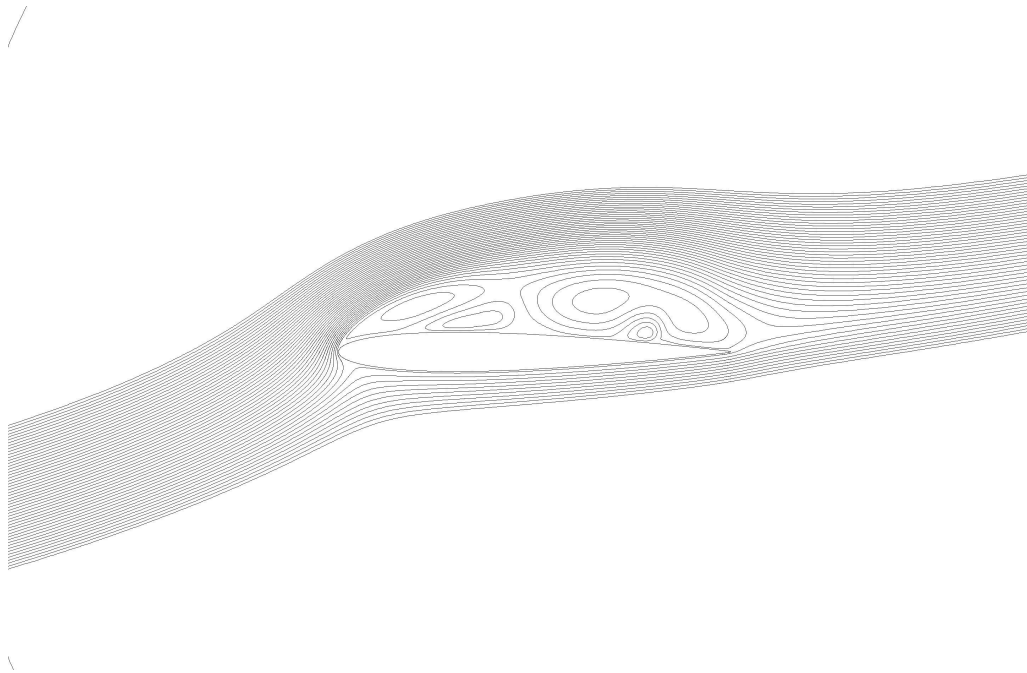
Figure 6.5: Streamlines for 0.25c and 0.75 actuators on.

When the third actuator is powered, the airflow reattaches completely but for a region in the leading edge (figure 6.6). This frotal stall is known to appear in thin wings previous to stall, and the placement of a new actuator to counteract this

effect was studied. The bubble was reduced but it did not dissapeared completely (figure 6.7). The stagnation points are seen more clearly, and at the trailing edge the air exits smoothly. The pressure gradients are depicted in Appendix B, where the clean airfoil is completely stalled, 1 and 2 actuators on configurations have some stall recovery and 3 and 4 actuators on are completely reattached with the suction peak upfront.

Figure 6.6: Streamlines for 0.25c, 0.5c and 0.75c actuators on.
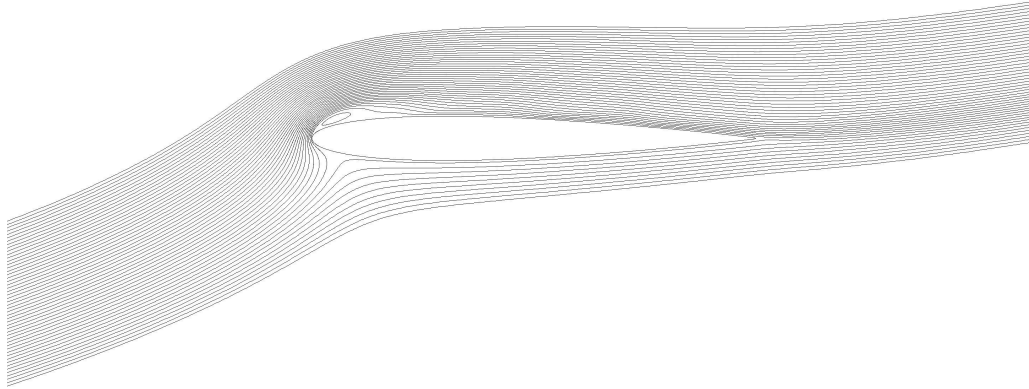
Figure 6.7: Streamlines for 0.1c, 0.25c, 0.5c and 0.75c actuators on.

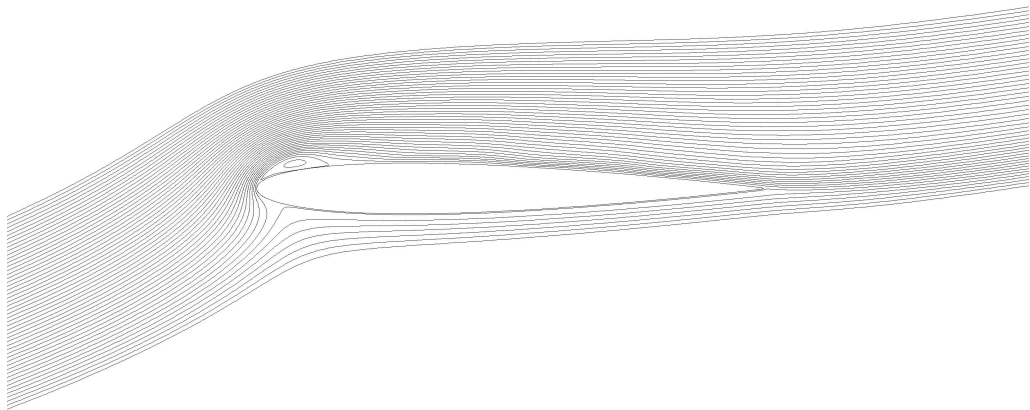Looking at the velocity profiles it is seen that the maximum velocity in all the volume increases as the actuators are being turned on. This is due to the reduction of the recirculation zone, and reacceleration once the fluid is reattached completely. As previous study has shown, the actuators cannot inflict that increase in the maximum velocity by themselves. The maximum velocity for no actuators case (figure 6.8) is around 13 m·s^{-1}, it increases to 15.5 m·s^{-1} (figure 6.9) for one actuator on and to 16 m·s^{-1} (figure 6.10) with two actuators. The actuators are clearly seen acting on the boundary layer, increasing the velocity on the points they are placed.
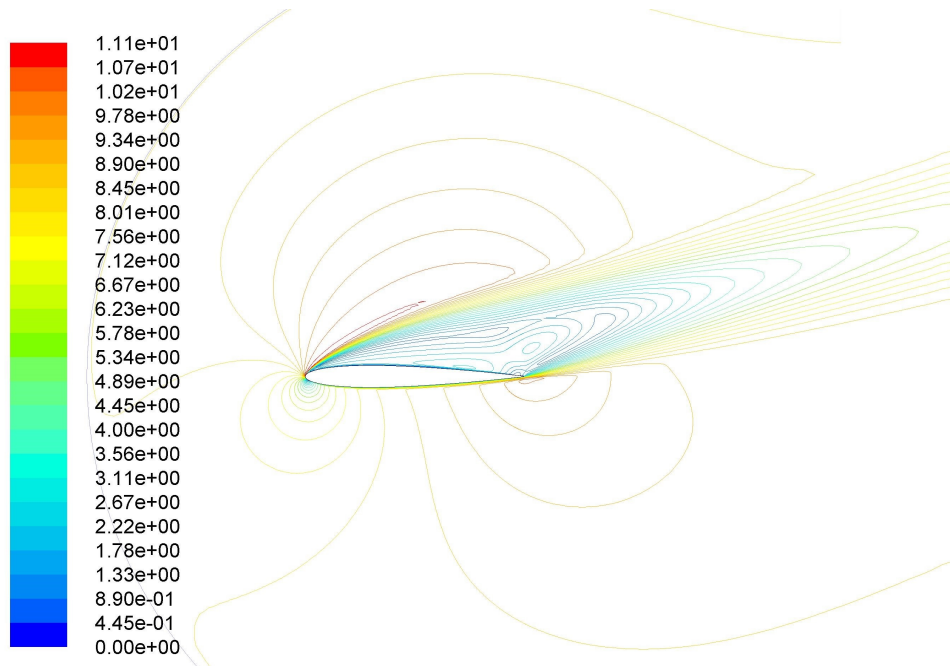
Figure 6.8: Velocity contours [m·s^{-1}] for no actuator on.
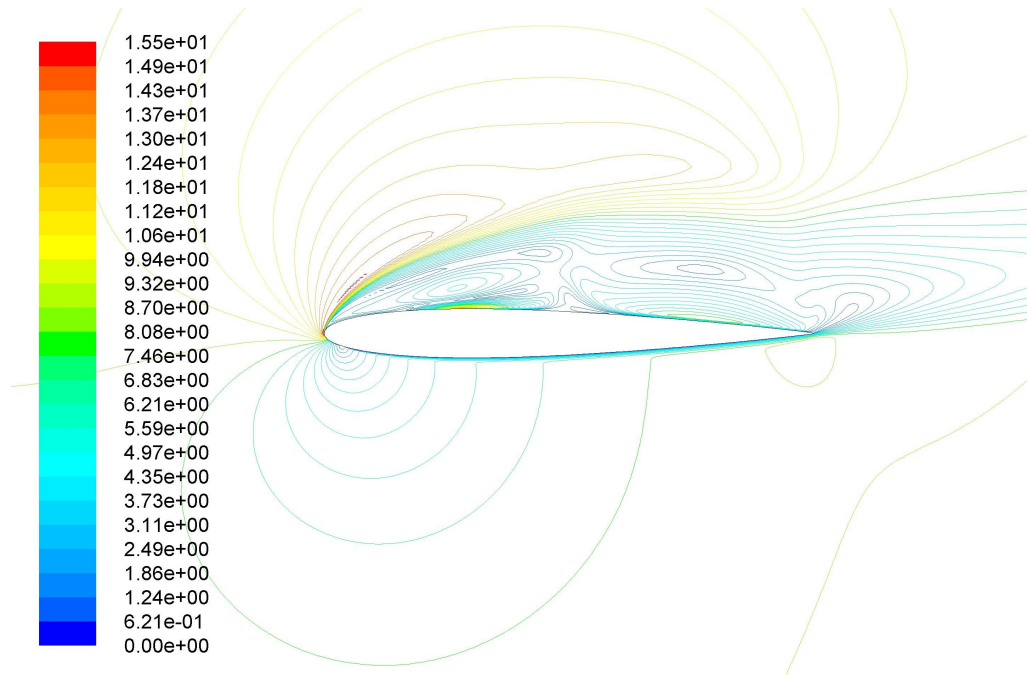
Figure 6.9: Velocity contours [m·s^{-1}] for 0.25c actuator on.
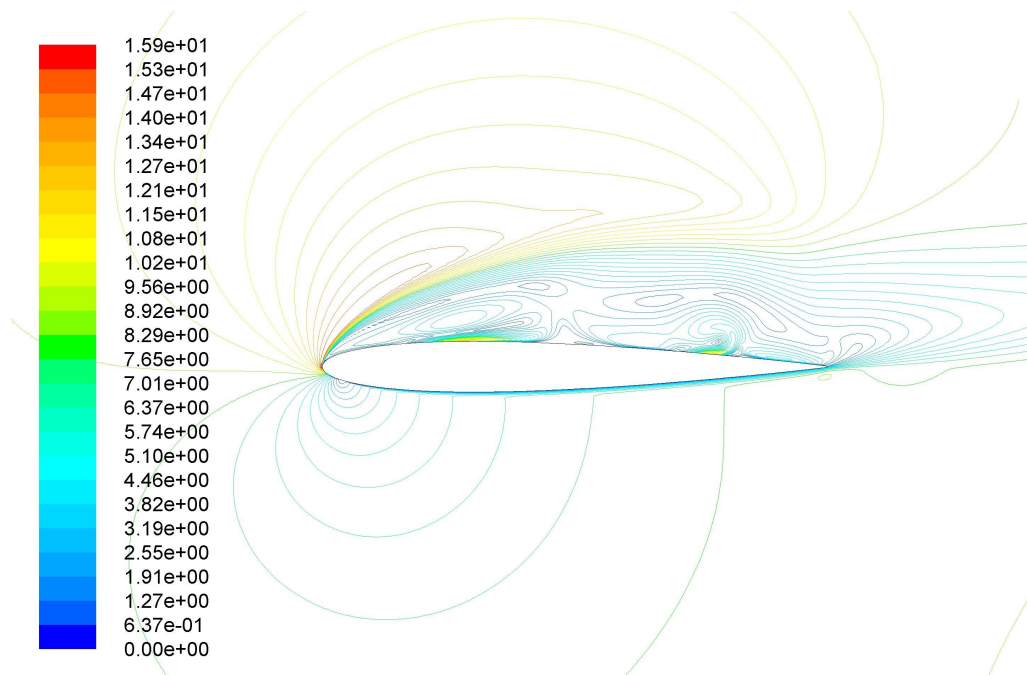
Figure 6.10: Velocity contours [m·s^{-1}] for 0.25c and 0.75 actuators on.

When the bubble reattaches, maxima velocities of up to 22.5 m·s^{-1} are presented. As expected, once the flow reattaches and the frontal actuator is turned on, the

maximum speed increases more like previously seen curves, increasing the maximum speed up to 24.2 m·s^{-1}.

The front actuator placed at 0.1c is however not able to produce a downstream movement of the air, but rather stop the air that is reflowing allowing for the rest of the actuators to accumulate better the effect, as well as to increase the velocity over the frontal actuator. This could be a detrimental factor for higher speed flows that need more energy to counteract reflow.
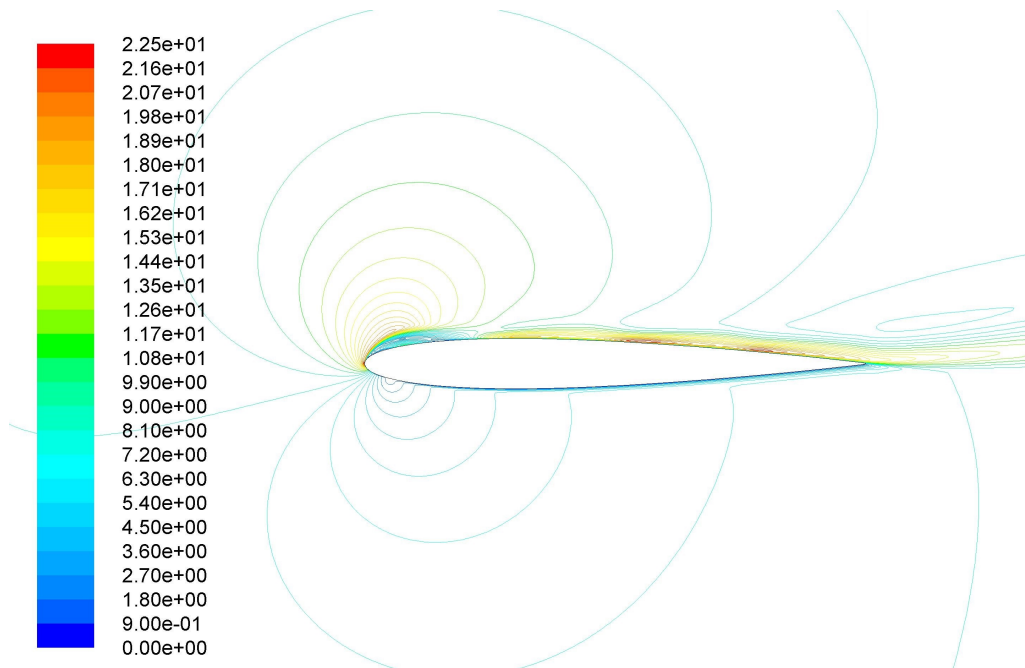
Figure 6.11: Velocity contours [m·s^{-1}] for 0.25c, 0.5c and 0.75c actuators on.
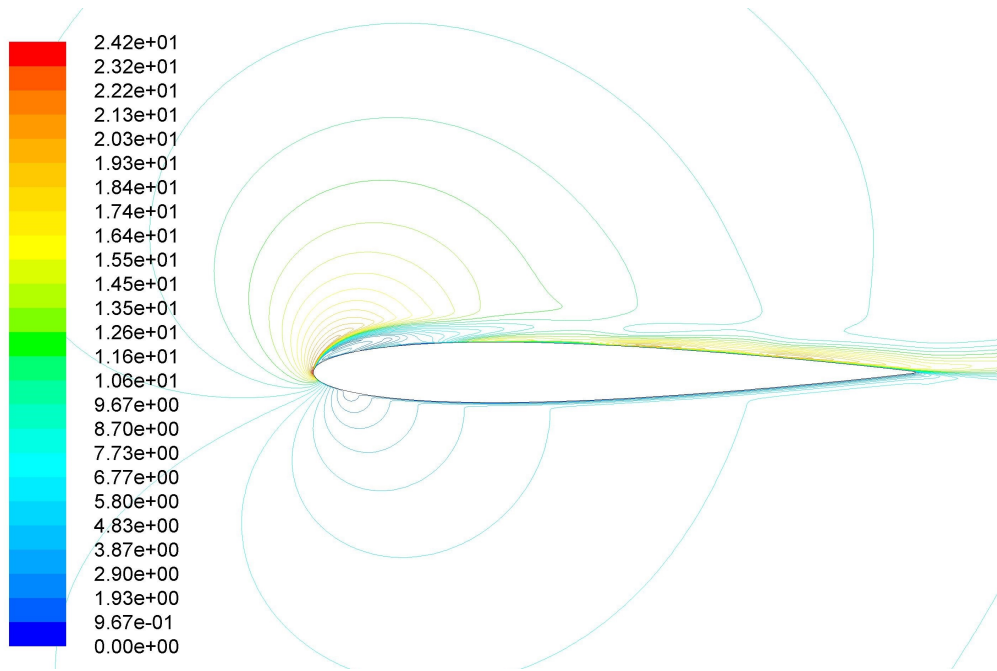
Figure 6.12: Velocity contours $[\text{m·s}^{-1}]$ for 0.1c, 0.25c, 0.5c and 0.75c actuators on.

The velocity vectors of the fluid were also extracted to be able to distinguish the direction of the fluid inside the stalled regions. The no actuators case (figure 6.13) shows only one recirculation pattern flowing clockwise, while for the 0.25c actuator (figure 6.14) the recirculation zone is split into three zones: a small frontal recirculation zone, a counter-clockwise recirculation zone just on top of the actuator and a larger clockwise zone downstream. This is the main reason the bubble is smaller, as the actuator disrupts the natural movement of the air.
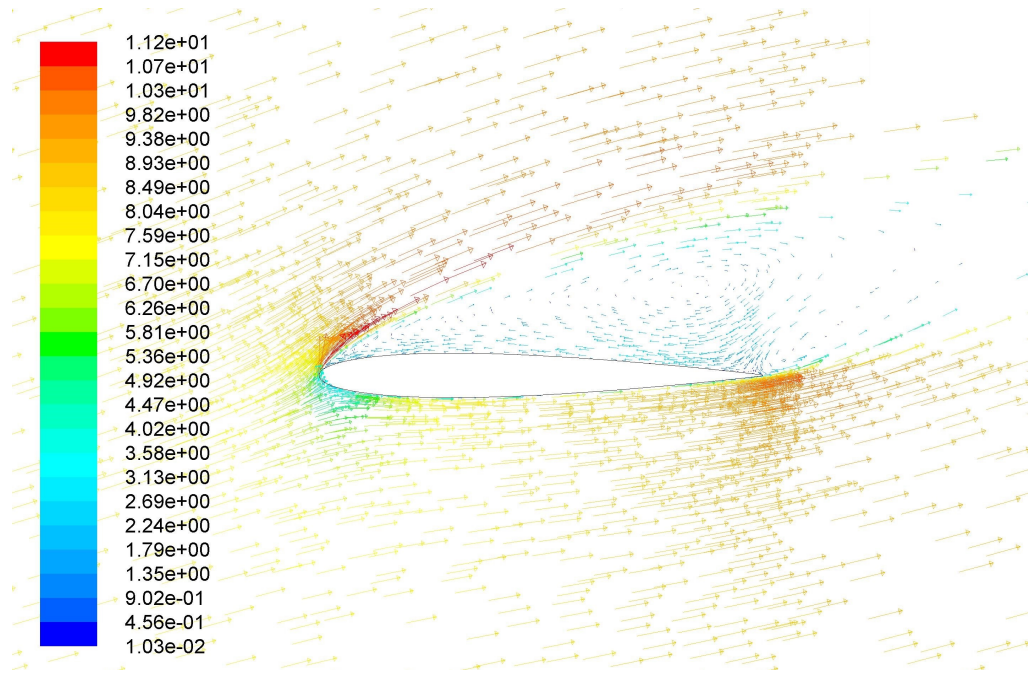
Figure 6.13: Velocity vectors [m·s^{-1}] for no actuator on.
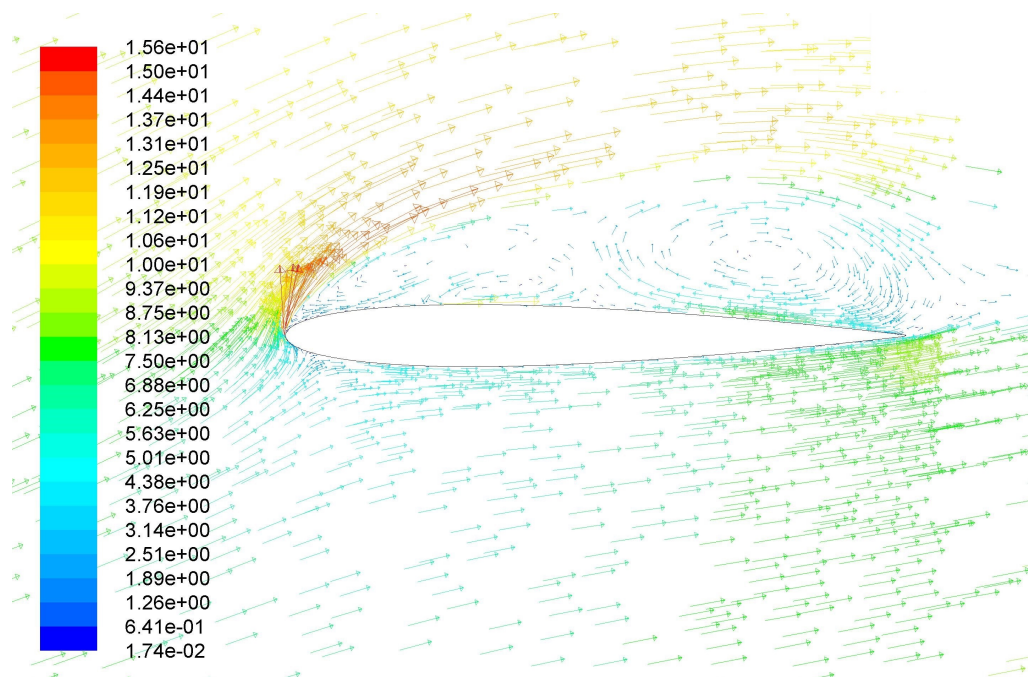
Figure 6.14: Velocity vectors [m·s^{-1}] for 0.25c actuator on.

The same happens when two actuators are powered, further reducing the bubble (figure 6.15) until the bubble dissapears once the three actuators are powered (figure

6.16). No further improvement is shown when a fourth actuator is powered (figure 6.17).
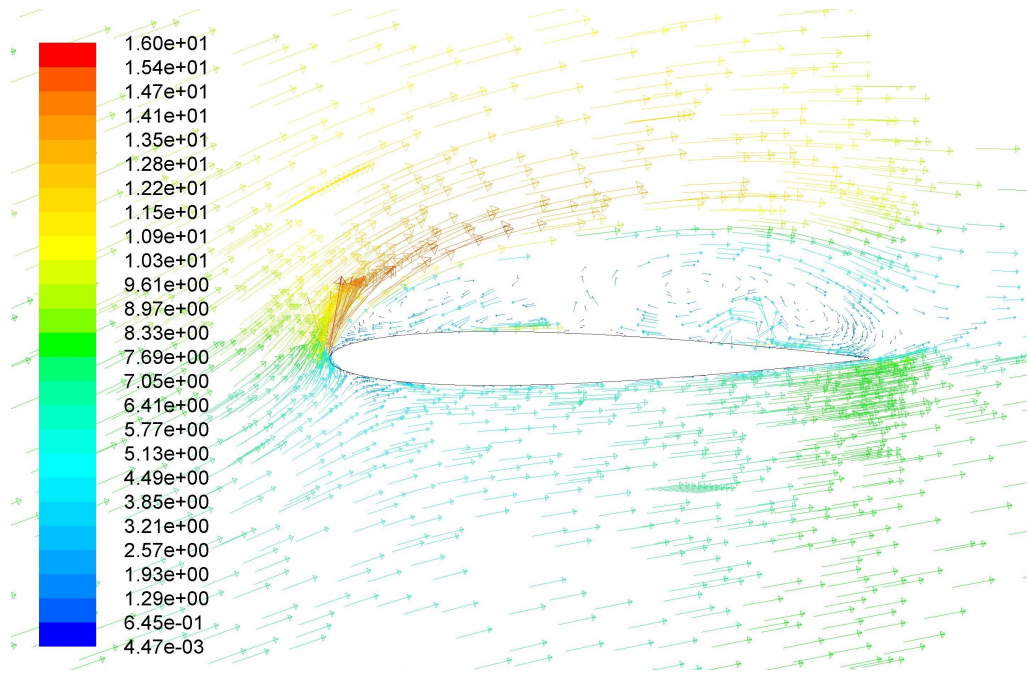
Figure 6.15: Velocity vectors [m·s^{-1}] for 0.25c and 0.75 actuators on.
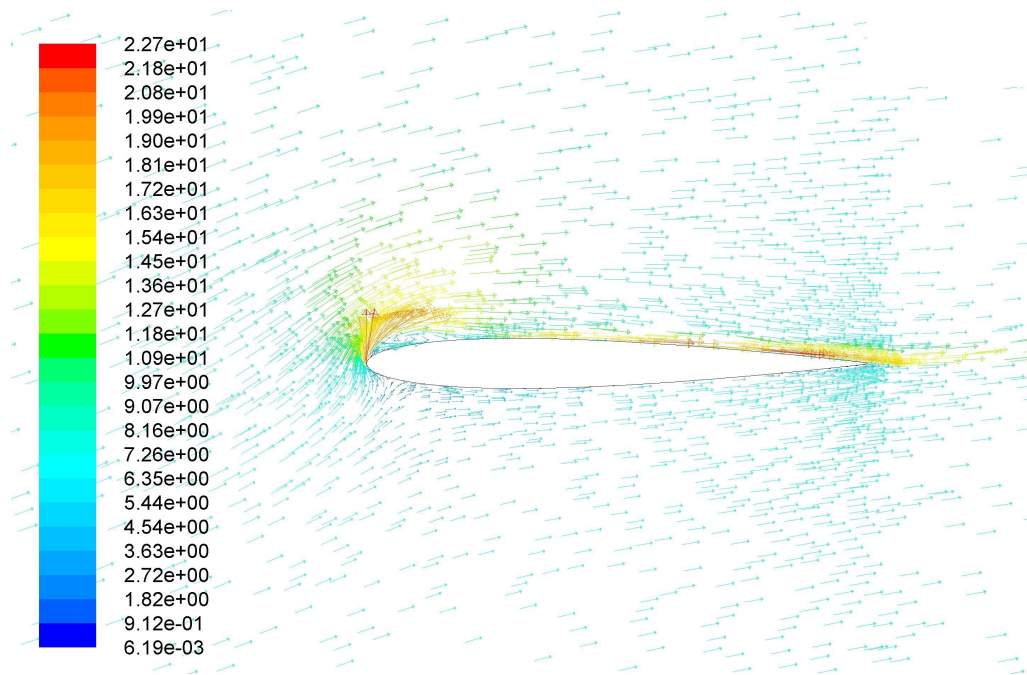
Figure 6.16: Velocity vectors [m·s^{-1}] for 0.25c, 0.5c and 0.75c actuators on.
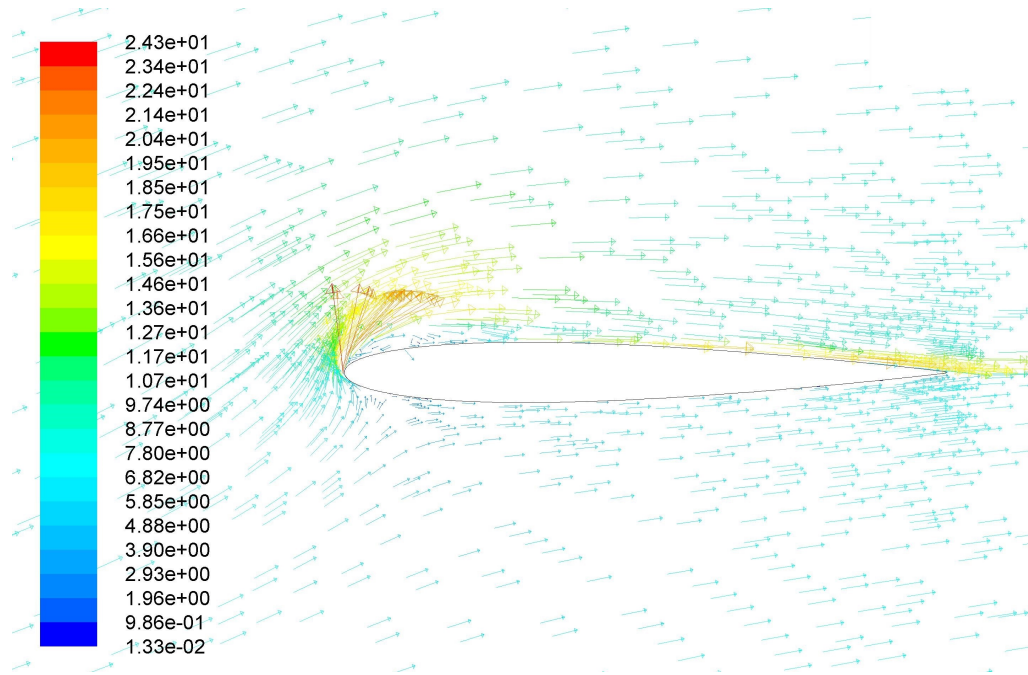
Figure 6.17: Velocity vectors [m·s^{-1}] for 0.1c, 0.25c, 0.5c and 0.75c actuators on.
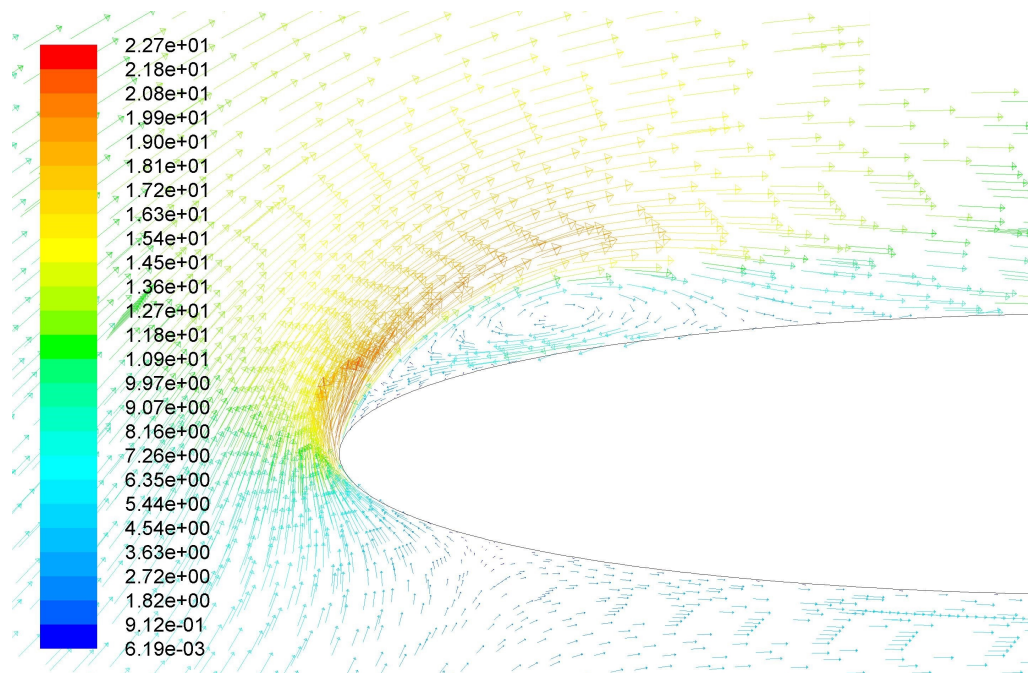
Figure 6.18: Velocity vectors [m·s^{-1}] for 0.25c, 0.5c and 0.75c actuators on, focusing on the frontal bubble.

Analyzing the forces that act on the airfoil (table 6.2) it is seen that for no actuators powered the lift coefficient of the airfoil is around 0.794. When the actuators

are powered, they produce a little thrust that is enough to counteract the drag produced in the y direction. This is, however, not the drag that the entire frame suffers, as effects for induced drag have to be taken into account.

Configuration	C_l	C_d	$C_{l\alpha}$
Clean	0.7940	0.04587	2.8433
1 actuator	2.1817*	-0.05057	7.8126
2 actuator	2.2068*	-0.06430	7.9026
3 actuator	1.9221	-0.23750	6.8830
4 actuator	2.1220	-0.30949	7.5989

Table 6.2: Forces applied to the airfoil. *marks an unsteady case solution, and data is not reliable to full extent.

The actuators produce a relevant effect when they are applied to an airfoil subjected to low Reynolds number flow. Even if they are not able to fully reattach the fluid to the surface, they are acting fairly on the flow and reducing considerably the skin friction drag. It is shown that increasing the number of actuators implemented over a surface the stronger is the action on the flow.

When one actuator is implemented the recirculation zone is reduced but still remains. When four actuators are operated, the fluid completely reattaches and no recirculation pattern above the airfoil remains. However, a weak leading edge vortex remains, that can be further reduced by adding at its location an actuator. The trailing edge stall has been completely cancelled.

The actuators are able to counteract the drag forces over an airfoil due to viscosity effects, creating some force in the opposite direction.

Conclusions and perspectives

In this chapter the main conclusions extracted from the work are summed up. A brief pointing towards future work and development on the topic will be commented as well.

7.1 Conclusions

The objectives of the present work were to study and validate a simplified model to predict the action of a DBD plasma actuator on the air and its effects, integrating it on a CFD platform and developing different appplciations.

- The merged model provides reliable solutions regarding flow prediction, and behaves in a similar manner to the experiments carried out. The model overcomes part of the defficiencies from their origins making it more complete, although it inherents others that induce inaccuracies.

- There is an accumulation effect on the velocity when several actuators are placed in-series, as well as an accumulation of momentum that is transferred to the upper layers by shear stresses. The accumulation of momentum has a strong dependency on the length of the actuator used, as a more gapped actuator may distribute the force in a more efficient manner.

- The increase of frequency of the actuators of five times almost doubles the force imparted by the actuator. The accumulation effect for the actuators is 50%.

- The model is also able to predict the behavior of a more complex structure such as a synthetic jet. This jet has shown to have an strong dependency on the separation of the actuators, needing an optimization of distance to obtain the maximum thrust.

- The model is able to reproduce other behaviors such as tilting and recirculation of tilting jets. Changing the applied voltages to one of the actuators shows this effect, that could also be changed by changing the frequency. There is a limit angle where the jet no longer hold in the desired direction and bends towards the limited actuator. The greater contribution to the momentum of the jet comes from the most powered actuator.

- An arragement of actuators may be able to recover from stall at high angles of attack with low speeds. Even if a complete reattachment of a recirculation zone is not possible, it is reduced by the use of an actuator by breaking it in several smaller zones.

- The actuators are able to reduce the skin friction drag in the direction they are blowing, effectively creating a negative drag.

7.2 Future work

Taking into account this considerations, the model may be improved by refitting Singh distribution of force for other actuator geometries to give a complete behavior to the model. Then, the actuators may be used to study other flow configurations such as high Reynolds number flows.

The model is able to predict some behaviors, which allows to drop the coupling between Poisson's an Navier-Stokes equations and reducing computational costs. This model, however, does not take into account any thermal effect, that could have an influence on the behavior of the fluid changing the turbulence behavior.

The model should be validated as well for a 3D behavior, as it could have an impact on vortex generation for aerodynamic control of high sweep-angle wings. Regarding the possible applications of the actuators it is important to assess high Reynold's number flows, and larger geometries involved. Other field of application in which the actuators may be used is the reduction of noise of exposed bodies to the fluid such as landing gears.

Once the model is implemented and a useful application found, the problems of integration and power generation may arise.

Project budget and legal framework

In this appendix a socioeconomic framework will be stablished in order to study the viability of the project. For this matter, a study on the project budget on the work already done will be performed.

A.1 Project budget

The costs of the project are specified below:

- **Computer system:** The computer employed was a universities computer. It was equiped with an Intel i7 processor and Windows 7 OS. The total estimated cost of said system and peripherals summed up to **800 €**.

- **ANSYS Fluent license:** This license is priced at **29,530 €** per license and **5,512 €**. However, other cheaper alternatives may be used (with other complications such as UDF implementation), like OpenFoam.

- **Man hours:** The cost of a junior engineer is 10 €/h. If it is considered that the work on the project has been of 330+ hours, then the total amount of man labour ascends to **3,300 €**.

- **Other costs** Such as electricity consumption of computers. Regarding that a computer runs uninterruptedly for two months, and considering it consumes up to 500 W, then the electricity consumed is the equivalent to around 744 kW·h. Assuming a cost of 0.13 €/kW·h, the cost of electricity is **100 €**.

These costs are all summed up in table A.1.

Concept	Amount [€]
Computer system	800
ANSYS Fluent license	35,042
Man hours	3,300
Others	100
Total	**39242 €**

Table A.1: Cost estimations

A.2 Legislation

For the modelling-validation phase no regulations apply. However, for future works on experimental setups the following regulations and remarks should be taken into account:

- **High Voltage:** The equipment involved in the actuators generate high voltages that could lead to high current discharges. For this purpose, regulations on protection against high voltages apply when involving and handling high voltage equipment. In Spain, Real Decreto 614/2001 regulates the operations involving high-tension devices, which due to the lack of proper handling prevented from obtaining an original set of experimental data.

- **High frequency:** Although the equpment involved may generate radio interference due to the high frequencies involved on its operations, the EASA regulations do not specify any regulations for these devices. EASA regulations only impose "Electronic isolation to prevent radiofrequency" distortion on directive 216/2008 and its ammendments, making it compulsory to revise the distortion these devices induce in the communications.

- **Chemical reactions:** The creation of plasma generates oxygen and nitrogen ions. These ions may be considered harmful for the environment, like NO_x or O_3^-. While these species last very short times in open air or have very low concentrations, they may be harmful when operated in closed environments.

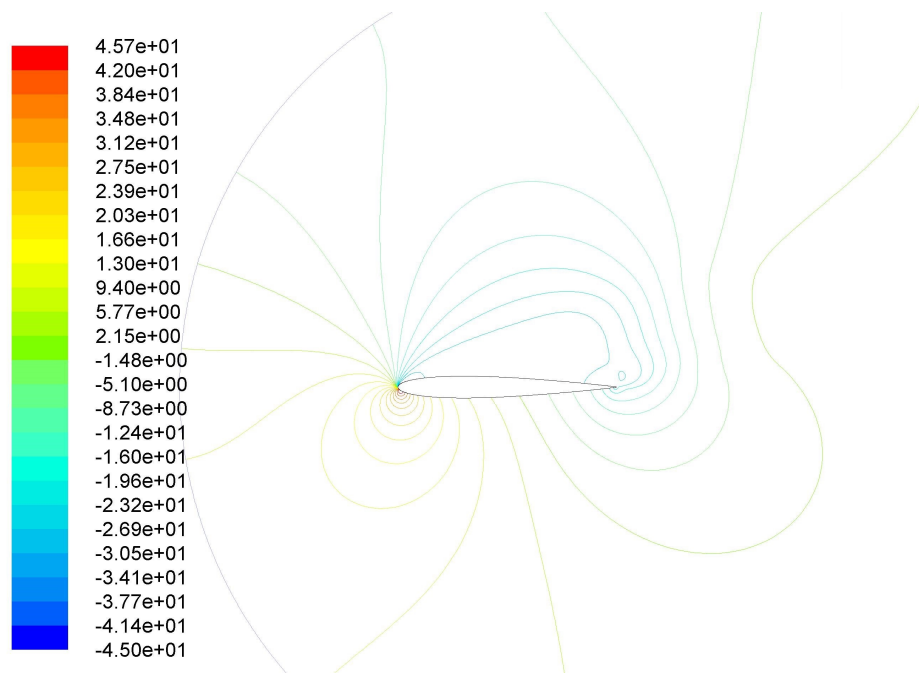# Figures of pressure contour maps of the airfoil actuators

Figure B.1: Contour pressures for clean configuration of the airfoil. Pressure is shown in Pascals.
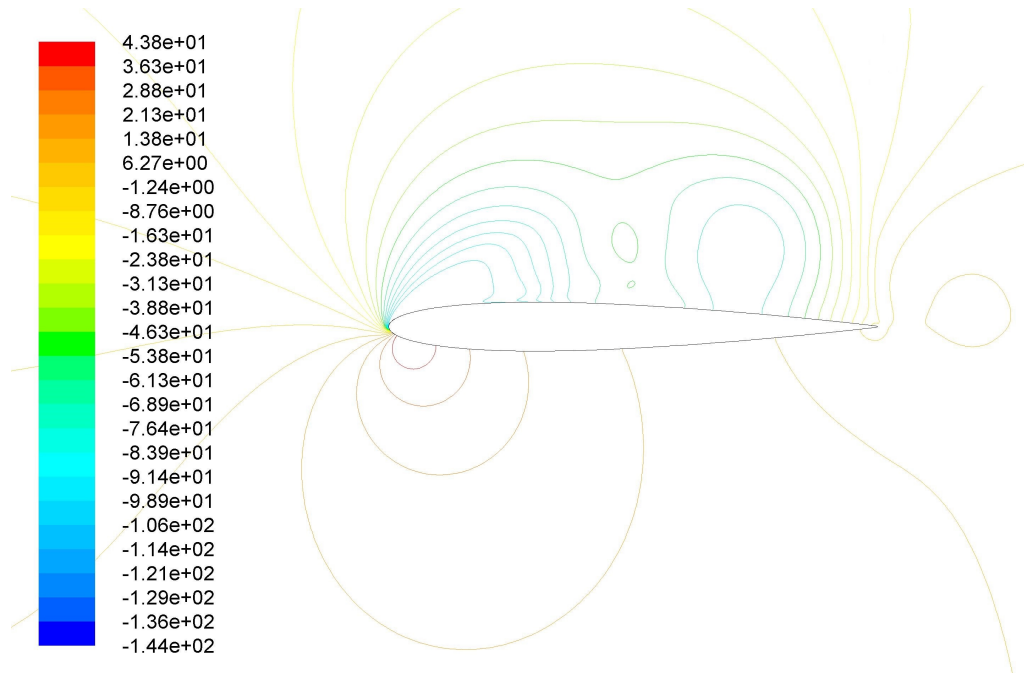
Figure B.2: Contour pressures for 0.25c actuator powered on configuration of the airfoil. Pressure is shown in Pascals.
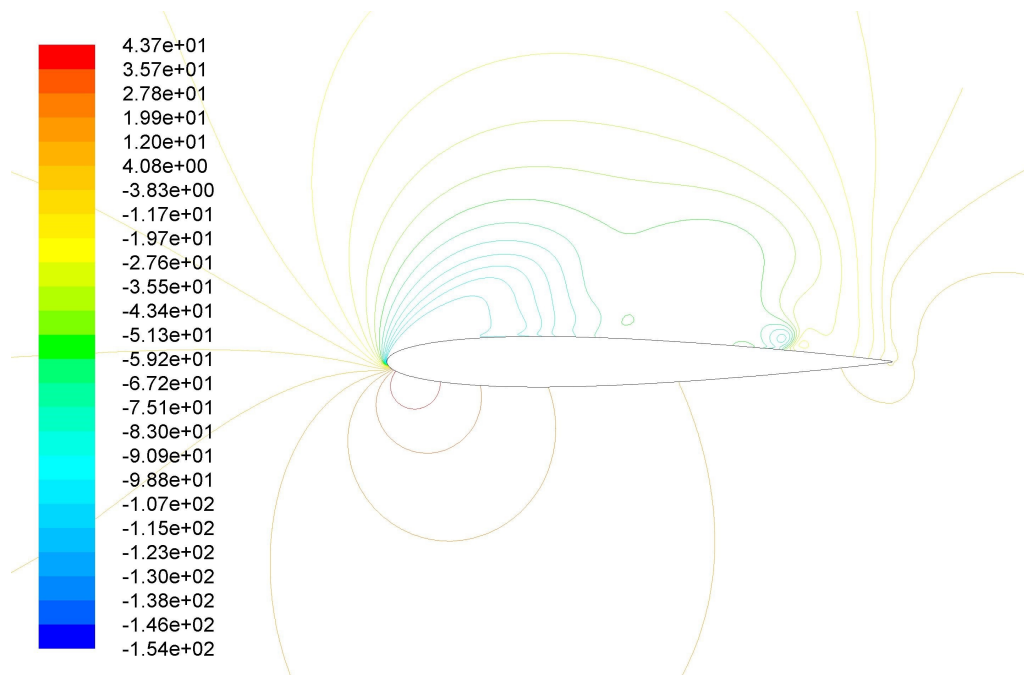

Figure B.3: Contour pressures for 0.25c and 0.75c actuators powered on configuration of the airfoil. Pressure is shown in Pascals.
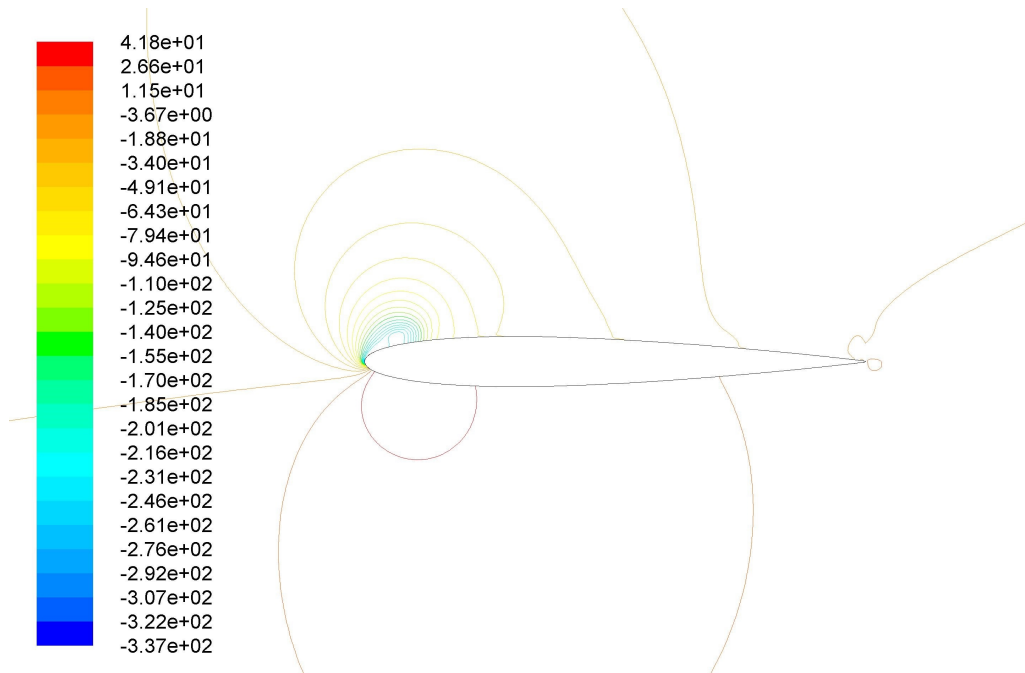
Figure B.4: Contour pressures for 0.25c, 0.5c and 0.75c actuators powered on configuration of the airfoil. Pressure is shown in Pascals.
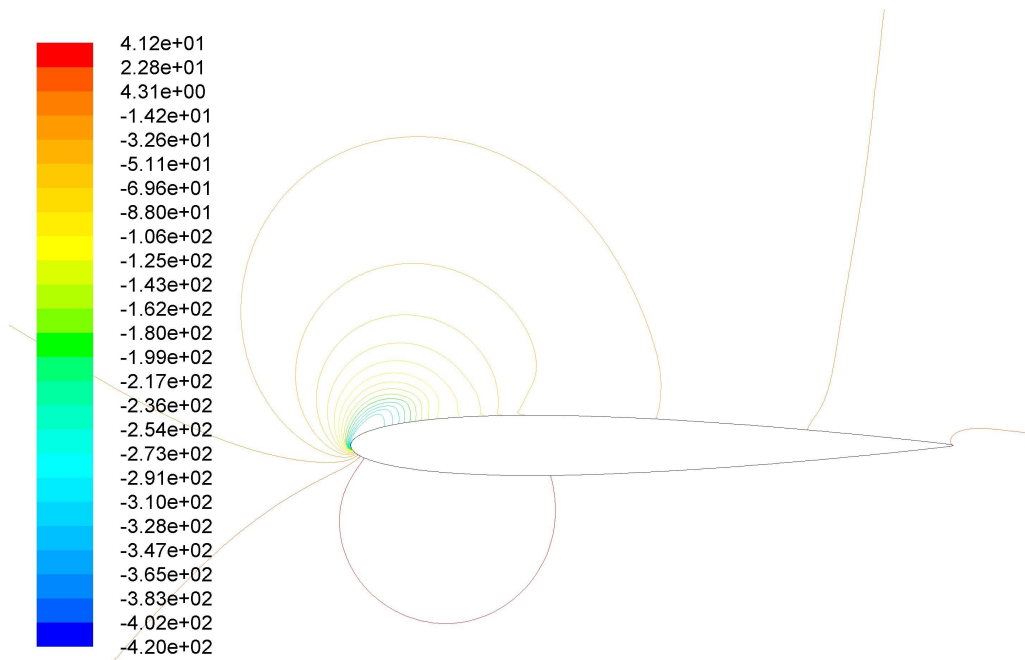

Figure B.5: Contour pressures for 0.1c, 0.25c, 0.5c and 0.75c actuators powered on configuration of the airfoil. Pressure is shown in Pascals.

Bibliography

[1] V. R. Soloviev. Analytical estimation of the thrust generated by a surface dielectric barrier discharge. *J. Phys. D: Appl. Phys.*, 45, 2011.

[2] E Moreau, A Debien, N Bénard, T Jukes, R Whalley, KS Choi, A Berendt, J Podlinski, and J Mizeraczyk. Surface dielectric barrier discharge plasma actuators. *ERCOFTAC Bull*, 94(5), 2013.

[3] M. Bolitho. *Jet Vectoring and Vorticity Generation Using Plasma Actuators*. PhD thesis, Oklahoma State University, May 2008.

[4] J Reece Roth. Aerodynamic flow acceleration using paraelectric and peristaltic electrohydrodynamic effects of a one atmosphere uniform glow discharge plasma. *Physics of Plasmas (1994-present)*, 10(5):2117–2126, 2003.

[5] CL Enloe, Thomas E McLaughlin, Robert D Van Dyken, KD Kachner, Eric J Jumper, and Thomas C Corke. Mechanisms and responses of a single dielectric barrier plasma actuator: plasma morphology. *AIAA journal*, 42(3):589–594, 2004.

[6] Flint O Thomas, Alexey Kozlov, and Thomas C Corke. Plasma actuators for cylinder flow control and noise reduction. *AIAA journal*, 46(8):1921–1931, 2008.

[7] Alexandre V Likhanskii, Mikhail N Shneider, Dmitry F Opaits, Richard B Miles, and Sergey O Macheret. Numerical modeling of dbd plasma actuators and the induced air flow. *AIAA paper*, 4533, 2007.

[8] V. R. Soloviev and V. M. Krivtsov. Surface barrier discharge modelling for aerodynamic applications. *J. Phys. D: Appl. Phys.*, 42, 2009.

[9] W. Shyy B. Jayaraman; and A. Andersson. Modeling of glow discharge-induced fluid dynamics. *Journal of Applied Physics*, 92(11), 2002.

[10] Balaji Jayaraman and Wei Shyy. Modeling of dielectric barrier discharge-induced fluid dynamics and heat transfer. *Progress in Aerospace Sciences*, 44(3):139–191, 2008.

[11] K. P. Singh and S. Roy. Force approximation for a plasma actuator operating in atmospheric air. *Journal of Applied Physics*, 103, 2008.

[12] L. del Amo. *Boundary layer mitigation by means of plasma actuators.* PhD thesis, Carlos III University, September 2015.

[13] L. Barbato. *Flow control using DBD plasma actuators: experimental investigation.* PhD thesis, von Karman Institute for Fluid Dynamics, June 2010.

[14] Boeuf J P; Lagmich Y; Unfer Th; Callegary Th and Pichford L C. Electrodynamic force in dielectric barrier discharge plasma actuators. *J. Phys. D: Appl. Phys.*, 40, 2007.

[15] Boeuf J P; Lagmich Y; Callegary Th; Pichford L C and Unfer Th. New insights in the physics of dbd plasma actuators for flow control. In *AIAA Meeting (Reno, NV, January 2008) AIAA Paper*, 2008.

[16] Eric Moreau. Airflow control by non-thermal plasma actuators. *Journal of Physics D: Applied Physics*, 40(3):605, 2007.

[17] Y Sung, W Kim, MG Mungal, and MA Cappelli. Aerodynamic modification of flow over bluff objects by plasma actuation. *Experiments in fluids*, 41(3):479–486, 2006.

[18] Nicolas Benard, Patrick Braud, Jerome Jolibois, and Eric Moreau. Airflow reattachment along a naca 0015 airfoil by a surface dielectric barrier discharge actuator—time-resolved particle image velocimetry investigation. *AIAA paper*, 4202, 2008.